Inorganic Chemistry

pubs.acs.org/IC

Article

First-Principles Calculations on Ni,Fe-Containing Carbon Monoxide Dehydrogenases Reveal Key Stereoelectronic Features for Binding and Release of CO_2 to/from the C-Cluster

Raffaella Breglia, Federica Arrigoni, Matteo Sensi, Claudio Greco,* Piercarlo Fantucci, Luca De Gioia,* and Maurizio Bruschi

Cite This: *Inorg. Chem.* 2021, 60, 387−402

Read Online

ACCESS | Metrics & More | Article Recommendations | Supporting Information

ABSTRACT: In view of the depletion of fossil fuel reserves and climatic effects of greenhouse gas emissions, Ni,Fe-containing carbon monoxide dehydrogenase (Ni-CODH) enzymes have attracted increasing interest in recent years for their capability to selectively catalyze the reversible reduction of CO_2 to CO ($CO_2 + 2H^+ + 2e^- \rightleftharpoons CO + H_2O$). The possibility of converting the greenhouse gas CO_2 into useful materials that can be used as synthetic building blocks or, remarkably, as carbon fuels makes Ni-CODH a very promising target for reverse-engineering studies. In this context, in order to provide insights into the chemical principles underlying the biological catalysis of CO_2 activation and reduction, quantum mechanics calculations have been carried out in the framework of density functional theory (DFT) on different-sized models of the Ni-CODH active site. With the aim of uncovering which stereoelectronic properties of the active site (known as the C-cluster) are crucial for the efficient binding and release of CO_2, different coordination modes of CO_2 to different forms and redox states of the C-cluster have been investigated. The results obtained from this study highlight the key role of the protein environment in tuning the reactivity and the geometry of the C-cluster. In particular, the protonation state of His93 is found to be crucial for promoting the binding or the dissociation of CO_2. The oxidation state of the C-cluster is also shown to be critical. CO_2 binds to C_{red2} according to a dissociative mechanism (i.e., CO_2 binds to the C-cluster after the release of possible ligands from Fe_u) when His93 is doubly protonated. CO_2 can also bind noncatalytically to C_{red1} according to an associative mechanism (i.e., CO_2 binding is preceded by the binding of H_2O to Fe_u). Conversely, CO_2 dissociates when His93 is singly protonated and the C-cluster is oxidized at least to the C_{int} redox state.

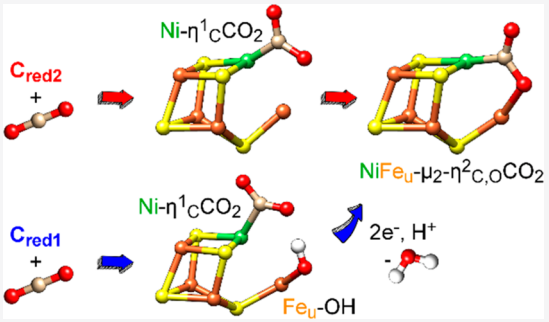

INTRODUCTION

Use of carbon dioxide as a carbon feedstock for the production of useful chemicals and fuels is considered one of the most promising approaches to overcome the limited supply of fossil fuels and simultaneously reduce the atmospheric concentration of greenhouse gases. Selective CO_2 reduction at low activation energy, however, is a critical challenge due to the high thermodynamic stability of the CO_2 molecule and the multielectron and multiproduct nature of the reduction process. For the development of large-scale and eco-friendly processes for CO_2 conversion, efficient and selective electrocatalysts based on inexpensive metals are therefore required. In this context, biological systems involved in the reductive assimilation of CO_2 to organic carbon may be a source of inspiration. In particular, a deep understanding of the chemistry performed by carbon monoxide dehydrogenases (CODHs), evolved over millions of years to efficiently catalyze the otherwise difficult two-electron reduction of CO_2, may be extremely useful to design novel and sustainable bioinspired catalysts for high-performance CO_2 to CO conversion.

Two chemically distinct types of CODHs are distinguished by their distribution and metal composition. The first of these is the O_2-sensitive enzyme from obligate anaerobic bacteria and archaea containing a highly asymmetric [Ni-Fe-S] cluster. This enzyme catalyzes CO oxidation with turnover frequencies (TOFs) of up to 40000 s^{-1} and CO_2 reduction with TOFs of 45 s^{-1}.[1,2] The second class of CODHs is the O_2-tolerant enzyme occurring in aerobic carboxidotrophic bacteria. They contain a bimetallic [Mo-(μ_2-S)-Cu] system that only catalyzes CO oxidation at a moderate TOF (100 s^{-1}).[3,4] The capability of Ni,Fe-containing CODHs (henceforth simply Ni-CODHs) to catalyze the reversible interconversion between CO_2 and CO

Received: October 12, 2020
Published: December 15, 2020

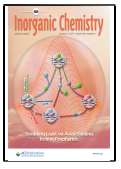

https://dx.doi.org/10.1021/acs.inorgchem.0c03034
Inorg. Chem. 2021, 60, 387−402

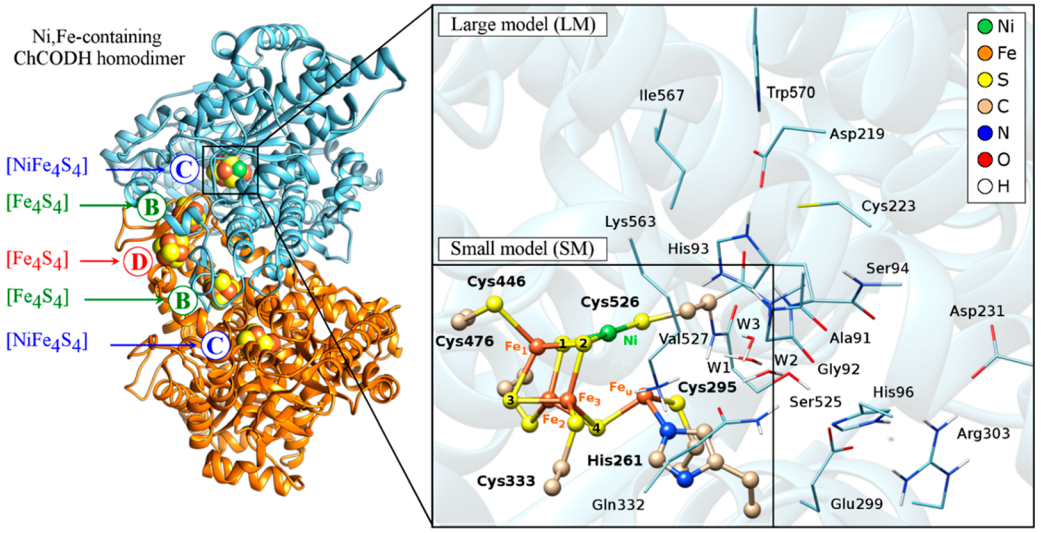

Figure 1. Cartoon representation of the X-ray crystal structure of the Ni-CODH homodimer from *C. hydrogenoformans* (PDB code 3B52). The C-cluster and its protein environment are shown enlarged on the right half of the figure. Atoms constituting the small DFT model (SM) are represented by a ball and stick representation, and corresponding residue names are indicated with bold labels; atoms also included in the large model (LM) are depicted as in a stick representation. Aliphatic hydrogen atoms and the CO_2 ligand bridging the Ni-Fe_u site in the 3B52 structure are not shown.

Scheme 1. Ni-CODH Catalytic Mechanism (in the Direction of CO_2 Reduction) Proposed by (a) Jeoung and Dobbek[5] and (b) Appel et al.[18,a]

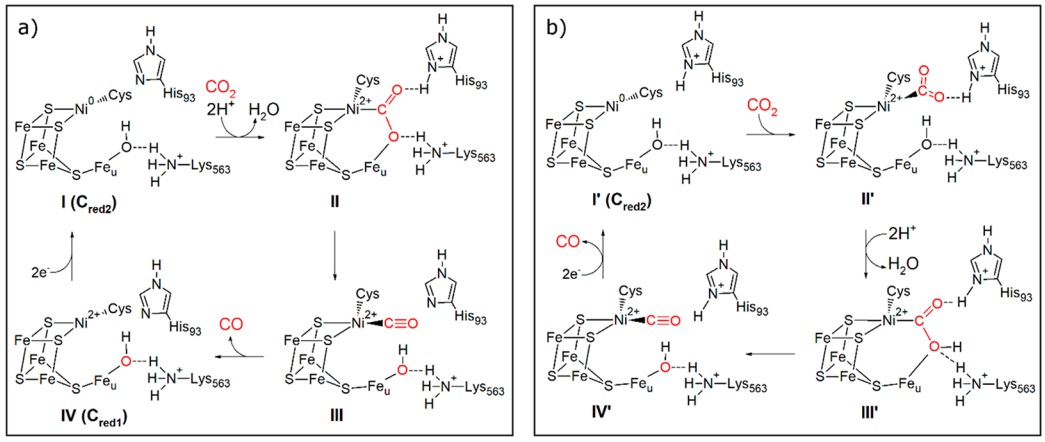

[a]Notably, in the first mechanism CO_2 binds to the C-cluster after the dissociation of a H_2O molecule from Fe_u (dissociative mechanism), whereas in the second mechanism CO_2 binds to Ni when a hydroxide ligand is still coordinated to Fe_u (associative mechanism).

has led researchers to spend increasing efforts in the study of these enzymes.

The Ni-CODH enzyme is a homodimeric protein of approximately 130 kDa with five metal clusters (see Figure 1).[5] Each subunit contains a $[Fe_4S_4]$ cubane (B-cluster) and an asymmetrical [Ni-Fe-S] cluster (C-cluster), at which the reversible CO_2 reduction occurs. An additional $[Fe_4S_4]$ cubane (D-cluster) is located at the interface between the two monomers. The Ni-CODH can also be a part of the heterotetrameric CO dehydrogenase/acetyl-coenzyme A synthase (CODH/ACS) complex, in which the reduction of CO_2 is coupled with the synthesis of acetyl-CoA in autotrophic and acetogenic bacteria,[6,7] or of the multimeric acetyl-CoA decarbonylase/synthase (ACDS) complex, in which the disassembly of acetyl-CoA is catalyzed for producing CH_4 in methanogenic archaea.

The Ni-CODH active site or C-cluster (see Figure 1), in both unifunctional and bifunctional enzymes, is covalently bound to the protein by five cysteine residues and one histidine residue. It is composed by an unusual structure formed by Ni, Fe, and S atoms; three Fe atoms and one Ni atom form a $[NiFe_3S_4]$ cluster, with a structure very similar to that of a "canonical" $[Fe_4S_4]$, in which an additional Fe atom extraneous to the cuboidal-like core (unique Fe or Fe_u) is inserted at an Ni−S edge. Three redox states of the C-cluster have been characterized by spectroscopic data: a fully oxidized inactive state (C_{ox}), an active state obtained from the monoelectronic reduction of C_{ox} (C_{red1}), and a state obtained from the bielectronic reduction of C_{red1} (C_{red2}). A further undetected diamagnetic state (C_{int}) is postulated to have an intermediate redox state between C_{red1} and C_{red2}. C_{ox} has the spin state $S = 0$ and exhibits a Mössbauer spectra typical of $[Fe_4S_4]^{2+}$ with no evidence of Fe_u.[8] Mössbauer parameters of the $S = 1/2$ C_{red1} state (g values at 2.01, 1.81, and 1.65, $g_{av} = 1.82$)[9] suggest instead high-spin Fe(II), Fe(II), Fe(III) formal oxidation states for the $[Fe_3S_4]$ subsite and the high-spin Fe(II) state for Fe_u,[8] whereas

https://dx.doi.org/10.1021/acs.inorgchem.0c03034
Inorg. Chem. 2021, 60, 387−402

L-edge X-ray absorption spectroscopy (XAS) indicates a low-spin diamagnetic Ni(II) ion.[10] The lack of ^{61}Ni hyperfine coupling in the C_{red1} EPR signal is consistent with a Ni site electronically isolated from the cluster that does not participate in the spin-coupling mechanism. The electronic structure of the paramagnetic C_{red2} state (g values at 1.97, 1.87, and 1.75; g_{av} = 1.86) is even more uncertain.[5,11−14] The similar EPR spectra of C_{red1} and C_{red2} suggest that the electronic structure of the $[Fe_3S_4]$ core fragment is unchanged, whereas Ni K- and L-edge XAS studies are consistent with a low-spin diamagnetic Ni(II) for both states.[10,15] However, the accommodation of two electrons at the Fe_u atom appears unlikely. On the basis of these considerations, two alternative descriptions of Ni in the C_{red2} state have been proposed: Ni(0) or the isoelectronic protonated site formulated as the nickel hydride species Ni(II)-H.[5,14]

CODH catalysis should involve the reductive conversion of the inactive C_{ox} state to C_{red1} and C_{red2}. Since C_{red1} and C_{red2} differ by two electrons and have an operational midpoint potential of −530 mV, which coincides with the values found for the CO_2/CO pair ($E^{\circ\prime}$ = −558 mV), they are respectively proposed as the redox states competent for CO oxidation and CO_2 reduction.[12,16] However, different mechanisms for the Ni-CODH catalytic cycle have been proposed due to the uncertainty in the oxidation states, the nature of the active ligands, and their coordination mode in C_{red1} and C_{red2}.[5,14,16−18] According to the Ni(II)/Ni(0) assignment for the Ni atom in the C_{red1}/C_{red2} state and Jeoung and Dobbek's high-resolution X-ray structures,[5,19] the catalytic mechanism reported in Scheme 1a has been proposed. It involves the formation of a nonbridging hydroxide ligand bound to the Fe_u atom in both active C_{red2} and C_{red1} states (see models **I** and **IV**, respectively) and a CO_2-bound intermediate in which CO_2 bridges the Ni-Fe_u site (model **II**). In the latter, the C atom is bound to the Ni atom, one O atom of the carboxylate group (O1) is coordinated to Fe_u and hydrogen-bonded to a conserved Lys residue, and the other O atom (O2) is H-bonded to a conserved His residue. On the basis of these structures, the binding of CO_2 to C_{red2} is proposed to take place via a dissociative mechanism (i.e. CO_2 binds the C-cluster after the dissociation from Fe_u of the hydroxide ligand as H_2O; see the **I** → **II** step in Scheme 1a). Subsequent cleavage of the C−O1 bond and transfer of a proton from the solvent to O1 via a series of His residues results, as very recently observed also by Liao and Siegbahn,[20] in the formation of a CO ligand and a OH^- ion, terminally bound to the Ni and the Fe_u atoms, respectively: an intermediate structurally related to model **III** in Scheme 1 has been actually proposed by the latter authors on the basis of DFT calculations. CO may then be released, with the C-cluster becoming oxidized by two electrons. Finally, two electrons are transferred, one at a time, from external electron donors through the D-cluster and the B-cluster to the C-cluster. This returns the C-cluster to C_{red2}.

A revised version of such a mechanism (see Scheme 1b) has been reported on the basis of information provided by biochemical experiments and X-ray diffraction studies of the *n*-butyl isocyanate inhibited enzyme.[21] This form, in which the inhibitor *n*-butyl isocyanate is terminally coordinated to Ni and an hydroxide ligand is terminally bound to Fe_u, is proposed to mimic a catalytic intermediate prior to the formation of the Ni−C−O1−Fe bridge (see model **II′** in Scheme 1b). According to this hypothesis, CO_2 terminally binds to the Ni atom through an associative mechanism when a hydroxide ligand is still coordinated to Fe_u (see the **I′** → **II″** step in Scheme 1b).

The oxidative addition of CO_2 to the Ni atom of the C_{red2} state featuring a hydride bound to the Ni(II) ion has also been proposed on the basis of combined structural and theoretical data.[14,17] However, also in this version of the Ni-CODH catalytic mechanism, there are many uncertainties about the binding of the CO_2 substrate to the C-cluster.

In order to shed more light on these aspects of the Ni-CODH catalytic cycle, quantum mechanical calculations have been performed on a minimal and a very large model of the active site. In particular, the CO_2 binding to the C-cluster has been investigated in the C_{red1}, C_{int}, and C_{red2} redox states, in the presence and in the absence of a hydroxide ligand bound to Fe_u. With the final aim of contributing to the provision of significant insights in unveiling the stereoelectronic and catalytic properties of the Ni-CODH enzyme, a detailed analysis of the geometries and electronic structures of relevant intermediates is also provided.

Results obtained from this study allow us to propose possible reaction mechanisms for the binding and release of CO_2 to/from the C-cluster. However, it should be pointed out that the latter are discussed only with consideration of minimum energy structures and, therefore, should be interpreted with care. Kinetic aspects, namely the prediction of transition states and the calculation of corresponding energy barriers, which must be considered for a complete and exhaustive mechanistic description of a reactive process, will be the object of a future work. The investigation described in the following indeed represents the initial step of a research line we are currently developing on the catalytic mechanism of Ni-CODHs.

METHODS

Models of the Ni-CODH Active Site. The starting structure for the DFT calculations was based on the X-ray geometry of the *Carboxydothermus hydrogenoformans* Ni-CODH (PDB code: 3B52),[5] in which a CO_2 molecule bridges the Ni and the Fe_u atoms of the active site. In the following, the residues are numbered according to this structure. In the framework of the cluster approach,[22−24] two models of different size (see Figure 1) have been considered to investigate the effect of the protein environment on the stereoelectronic properties of the active site of Ni-CODH.

The smallest model (SM), which contains up to 64 atoms, includes the $[Fe_4NiS_4]$ core of the C-cluster and the side chains of the residues forming its first coordination sphere (see the ball and stick representation in Figure 1, right). The five cysteine residues coordinated to the nickel and iron atoms (Cys295, Cys333, Cys446, Cys476, Cys526) and the histidine residue coordinated to the Fe_u atom (His261) are terminated at the Cα atoms and saturated with hydrogens. During the geometry optimization, terminal atoms are constrained to their crystallographic positions, in order to avoid unrealistic distortions of the C-cluster.

The largest model (LM) contains up to 234 atoms and has a size of 24 Å (see the stick representation in Figure 1, right). This model includes selected atoms of 16 residues belonging to the second coordination sphere (Ala91, Gly92, His93, Ser94, His96, Asp219, Cys223, Asp 231, Glu299, Arg303, Gln332, Ser525, Val527, Lys563, Ile567, and Trp570) and three water molecules, apart from all the atoms contained in the small model. In particular, the entire residue His93 and the side chain of Lys563 have been included in the model because they should be directly involved in the catalytic cycle, interacting with the ligands bounded to the C-cluster[5,19] and participating in acid−base reactions.[25,26] Notably, His93 is positioned at the top of a cationic tunnel composed of histidine residues located on sequential turns of a helix starting near the C-cluster and ending at the protein surface, which is proposed to facilitate transfer of protons during the reaction.[25,27] The importance of His93 and Lys563 in catalysis is confirmed by the loss of enzymatic activity after their

https://dx.doi.org/10.1021/acs.inorgchem.0c03034
Inorg. Chem. 2021, 60, 387−402

mutation.[27] Three protonation states are possible for His93 depending on whether δN, εN, or both atoms are protonated. Since the proton on δN strongly interacts with the carboxylate group of Asp219, it was always included in the model. Conversely, the proton on εN interacts with nonprotein ligands at the active site. Therefore, it is possible to assume that protonation state of εN plays a crucial role in the binding and release of the substrates. On the basis of these considerations, His93 has been modeled as either doubly protonated or singly protonated at the δN atom. Both protonation states of Lys563 (neutral and positively charged) have been also considered. The carbonyl and the Cα atoms of Ala91, the entire residue Gly92, and the N and Cα atoms of Ser94 have been included in the model because they form a small α-helix containing His93, whereas the side chain of Asp219 terminated at the Cα atom has been selected because its carboxylate group is H-bonded to His93. Conversely, the side chain of Trp570 terminated at the Cβ atom, interacting with Asp219, and the side chain of Cys223 terminated at the Cα atom have been included in the model in order to avoid unrealistic conformational changes of the side chain of His93. The side chain of Ile567 terminated at the Cα atom has been added to the model, since it is close to the vacant coordination site on Ni, whereas the side chain, the carbonyl and the Cα atoms of Ser525, and the N and the Cα atoms of Val527 have been selected because they form the peptide chain containing the residue Cys526, belonging to the first coordination sphere. Conversely, the side chain of Glu299 terminated at the Cα atom has been included in the model because it is H-bonded to Ser525. Finally, the side chains of His96, Gln332, and Cys223 terminated at the Cα atoms, the side chain of Arg303 truncated at the Cγ atom, the side chain of Asp231 terminated at the Cβ atom, and three water molecules, selected among those reported in the crystallographic structure, have been included in the model in order to mimic the entire H-bond network in the C-cluster environment. The truncated residues have been saturated with hydrogen atoms. During the geometry optimizations, 31 atoms have been constrained to the crystallographic positions, in order to avoid unrealistic distortions at the boundary of the model.

The Supporting Information contains a detailed list of the atoms composing the SM and the LM models and a list of the atoms that, during geometry optimizations, are fixed at their respective X-ray positions (see Table S1).

A medium model, containing up to 132 atoms, of the active site has also been considered in order to calculate zero-point energy corrections. It contains the [Fe_4NiS_4] cluster and the side chains and the Cα atoms of Cys295, Cys333, Cys446, Cys476, Cys526, His261, His93, Lys563, Asp219, and Ile567. Constrained-geometry optimizations of this medium model have been performed. Initially, all atoms with the exception of hydrogens were constrained at the positions computed for the large-sized model. Constraints were then progressively removed. Such a procedure allows us to obtain structures that best reproduce the geometries obtained with the large model and to compute consistent reaction energies.

Computational Details. Quantum mechanics (QM) calculations have been carried out in the DFT framework with the Turbomole program suite,[28] using the BP86 exchange-correlation functional[29,30] in conjunction with the resolution of the identity (RI) technique.[31] The BP86 functional is commonly used to study metal-containing molecular systems such as metallo-enzymes, due to the increasing available computational data which indicate that BP86 is one of the most accurate pure functionals to study transition-metal compounds.[32] BP86, coupled with an appropriate basis set, predicts reaction energies with a reasonable accuracy and reproduces experimental geometries within a few hundredths of an angstrom.[33] In the small model, an all-electron valence triple-ζ basis set with polarization functions (def-TZVP)[34] was used for all atoms. In the large model the def-TZVP basis set was used for the [Fe_4NiS_4] core of the C-cluster, the sulfur, and the Cβ atoms of Cys526 and all atoms of Cys295, Cys333, Cys446, Cys476, and His261. For all other atoms, the double-ζ basis set SVP[35] was used (for details, see Table S1). The BP86/def-TZVP level of theory for the representation of the metal-containing cofactor has been proved to be suitable for the reproduction of both electronic and structural properties of complex antiferromagnetically coupled bioinorganic systems; for example, it was proven to correctly describe the stereoelectronic properties of the Ni-Fe active site of Acetyl-CoA synthase[38] and of the chain of multiple-metal-containing redox-active sites embedded in FeFe-hydrogenases.[39] The effects of the protein environment have been modeled by placing the molecular cluster in a polarizable continuum medium with $\varepsilon = 4$, according to the conductor-like screening model (COSMO).[36,37]

In order to verify the consistency of the results, single-point energy calculations on the BP86-optimized geometries of relevant species along the CO_2 binding/dissociation pathway have been also carried out using different functionals: namely, B3LYP,[40−42] PBE0,[43] and M06.[44] The obtained results are consistent with those obtained by using the BP86-COSMO scheme; the reaction energies are similar and show the same trend with respect to the redox state of the C-cluster (see Table S2). BP86, B3LYP, PBE0, and M06 single-point energy calculations have been also performed by including the dispersion interaction correction given by the DFT-D3 Grimme scheme,[45−47] as implemented in Turbomole. Since the binding of CO_2 to the C-cluster involves the formation of a short metal−ligand bond, CO_2 binding energies could be sensitive to the spatial cutoff function. Therefore, D3 dispersion contributions were also calculated by applying the Becke−Johnson (BJ)-damping function.[48] Since the M06 functional is parametrized for the treatment of short- and medium-range correlation effects, it is incompatible with the BJ-damping function[49] and only the zero-damping function has been applied to it. Structure optimizations including dispersion corrections have not been performed because they have been shown to increase the deviation between DFT and experimental binding energies.[50] As shown in Table S2, for a given reaction, the inclusion of dispersion interactions in the calculations has a constant effect and it is independent of the redox state of the active site; when dispersion interactions are considered, CO_2 binding is always predicted to be more favorable. Conversely, the use of the BJ-damping function instead of the standard damping function has only a negligible effect on reaction energies. This result is in line with the work by Grimme and co-workers.[48] Zero-point energy corrections have been also computed for several species using the medium model of the active site. Notably, they are always lower than 3 kcal/mol for CO_2 binding and equal to zero for isomerization reactions (see Table S3). Additionally, for a given reaction, they are almost the same for the different redox states of the C-cluster. Therefore, for the sake of clarity, the results obtained by including dispersion and ZPE corrections will be not further commented on in the text.

In the framework of the single-determinant DFT approach, the antiferromagnetic coupling of the Fe atoms in the C-cluster has been treated within the spin-unrestricted broken-symmetry formalism (BS) introduced by Noodleman.[51] The resulting BS state is not a pure spin state but rather a mixed state in which the majority spin and minority spin are arranged either spin-up or spin-down to give a spin coupling pattern with the correct net total spin and an overall either antiferromagnetic or ferromagnetic alignment. To construct a desired BS state, a calculation of the high-spin state is first completed, which is a pure spin state described by a single determinant with all unpaired electrons aligned in the same direction (α spins) to adopt the highest possible total spin state. Subsequently, groups of occupied α and β MOs of the high-spin state are exchanged in order to generate a guess of the spin-flipped state which is obviously submitted to a DFT energy minimization. For instance, in the C_{red1} state a mixed-valence Fe(II,HS)Fe(III,HS) pair of spin $S = 9/2$ and a ferrous Fe(II,HS)Fe(II,HS) pair of spin $S = 4$ are coupled antiferromagnetically to give an overall low-spin ground state which exhibits an $S = 1/2$ EPR signal,[9,52] whereas the Ni atom is low-spin diamagnetic Ni(II).[10,15] The $S = 1/2$ BS state for C_{red1} has therefore been obtained by manipulating the density of the highest possible total spin state, $S = 17/2$. Analogously, the desired BS states for the one- and two-electron-reduced states, C_{int} ($S = 0$) and C_{red2} ($S = 1/2$), have been obtained from the $S = 18/2$ and $S = 19/2$ high-spin states, respectively. The resulting electronic structures of the six possible nonequivalent spin coupling schemes for the C-cluster (see Scheme S1) which satisfy $S = 1/2$ for C_{red1} and C_{red2} and $S = 0$ for C_{int} have been checked by computing Mulliken spin densities and NBO atomic charges.

https://dx.doi.org/10.1021/acs.inorgchem.0c03034
Inorg. Chem. 2021, 60, 387−402

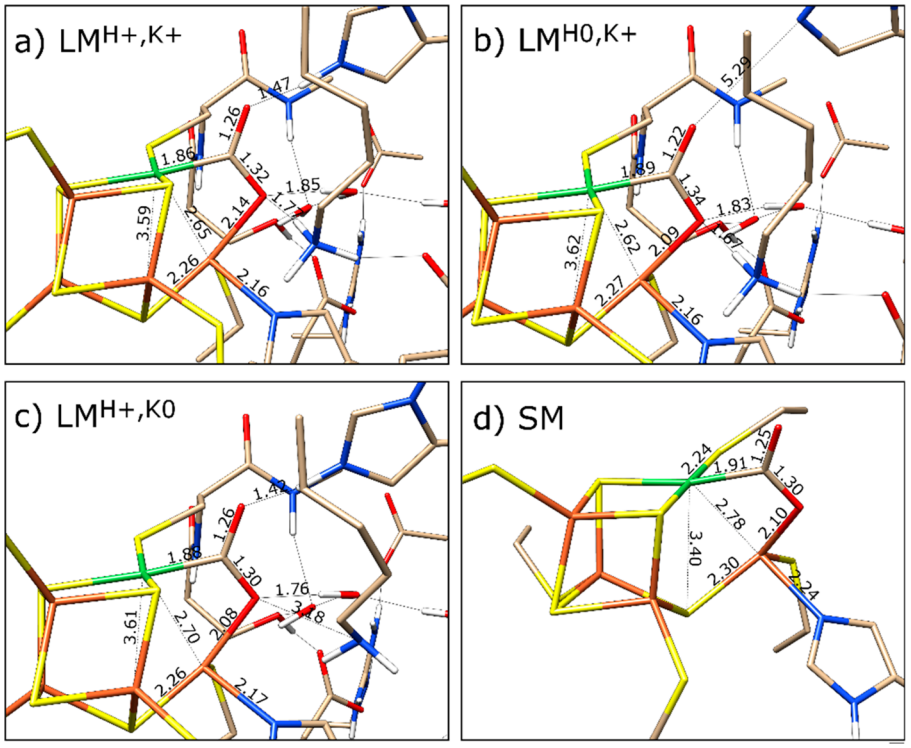

Figure 2. Schematic representation of the geometries of the μ-CO_2-bound form of the C-cluster in the C_{red2} state optimized using the (a) $LM^{H+,K+}$, (b) $LM^{H0,K+}$, (c) $LM^{H+,K0}$, and (d) SM models. Selected interatomic distances are given in Å. Aliphatic hydrogen atoms are not shown.

Since the resolution of the X-ray structures of the enzyme is not sufficiently high to establish the broken-symmetry state of the C-cluster, the geometries of all investigated species have been optimized according to all possible spin-coupling schemes using the SM model. The geometries of the different broken-symmetry states are very similar, whereas their relative stabilities are strongly influenced by the electronic structure of the C-cluster. In particular, the spin alignment patterns in which the Fe_1Fe_u pair is coupled antiferromagnetically with the Fe_2Fe_3 pair (BS-3 and BS-6 in Scheme S1) are always found to be of lower energy (see Table S4). On the basis of these results, geometry optimizations carried out using the large model of the active site have been performed by aligning the Fe site spin vectors according to only these two spin coupling schemes. All relative and reaction energies reported in this work have been calculated by considering the more stable BS state for each species involved. Analogously, geometries and electronic structures described in the Results refer to the more stable BS state.

Due to the uncertainty about the spin state of the EPR-silent C_{int} redox state, triplet ($S = 1$) and quintuplet ($S = 2$) spin states have been also considered for the more relevant species discussed in this work. Notably, as shown in Table S5, the singlet ($S = 0$) BS state is always more stable than higher-spin states (or at least isoenergetic with the triplet state) and, therefore, for the sake of clarity the latter states will be not further commented on in the text.

Nomenclature. In the following, computational models will be labeled according the general scheme **RS-X-KM**, where **RS** is the formal redox state of the C-cluster ($\mathbf{C_{red1}}$, $\mathbf{C_{int}}$, or $\mathbf{C_{red2}}$), **X** is the specific chemical nature of the ligand(s) bonded to the active site, and **KM** is the size of the model (**LM** or **SM**). The protonation states of His93 and Lys563 are indicated by the superscript after the **LM** label; **H+** and **K+** denote the positively charged states of His93 and Lys563, respectively, whereas **H0** and **K0** denote their neutral form. Energies of all species investigated in this work are reported in Table S6 in the Supporting Information.

RESULTS

Numerous X-ray structures of Ni-CODHs have been reported so far. Among these, two high-resolution crystal structures (PDB codes: 3B52 and 4UDX) feature a CO_2 molecule bound to the C-cluster.[5,19] In both structures, the carboxyl carbon atom of CO_2 is coordinated to the Ni ion (η^1(C) coordination), completing its distorted-square-planar geometry, whereas one carboxyl oxygen is bound to the Fe_u metal (η^1(O) coordination), resulting in a μ_2-η^2(C,O) binding mode of CO_2 bridging the Ni-Fe_u site (henceforth referred to as simply μCO_2). Although this is the only coordination mode that has been experimentally observed, in order to exhaustively explore the binding and dissociation mechanism of CO_2 to and from the C-cluster, other coordination modes have been investigated. Indeed, a new species in which CO_2 is terminally bound to the Ni atom through the carbon atom (hereafter referred to as tCO_2) has been identified as a genuine minimum on the PES. It may play a key role in the binding/dissociation of the CO_2 molecule to the C-cluster. In addition, the possibility that CO_2 may bind to the C-cluster according to an associative mechanism, with a binding mode similar to that observed for the *n*-butyl isocyanate inhibitor in the X-ray structure of *C. hydrogenoformans* CODH (PDB code: 2YIV),[21] prompted us to investigate the binding of CO_2 to the Ni ion in the presence of a hydroxide ligand bound to Fe_u. Such different binding modes of CO_2 have been investigated for the C_{red2}, C_{int}, and C_{red1} redox states of the C-cluster with different protonation states of the nearby His93 and Lys563 residues to disclose the crucial role of the protein environment in assisting the CO_2 binding.

***μ_2-η^2*(C,O) binding of CO_2 to the Ni-Fe_u Site of the C-Cluster.** The 3B52 CO_2-containing crystal structure has been solved at 1.5 Å from a sample poised at −600 mV (equivalent in its redox potential to the C_{red2} state) in the presence of HCO_3^- as the CO_2 source,[5] whereas the 4UDX structure, which was also

https://dx.doi.org/10.1021/acs.inorgchem.0c03034
Inorg. Chem. 2021, 60, 387−402

Table 1. Computed NBO Charges for the CO_2 Molecule Bound to the C-Cluster in μCO_2, tCO_2, and CO_2-OH, Calculated Using the $LM^{H+,K+}$, $LM^{H0,K+}$, $LM^{H+,K0}$, and SM Models of the Active Site

	μCO_2			tCO_2			CO_2-OH		
	C_{red2}	C_{int}	C_{red1}	C_{red2}	C_{int}	C_{red1}	C_{red2}	C_{int}	C_{red1}
$LM^{H+,K+}$	−1.03	−0.98	−0.91	−1.00	−0.92		−0.94	−0.80	−0.67
$LM^{H0,K+}$	−0.95	−0.88	−0.79	−0.73	−0.56	−0.37	−0.71	−0.61	−0.49
$LM^{H+,K0}$	−0.96	−0.91	−0.84				−0.87	−0.81	−0.69
SM	−0.98	−0.91	−0.82	−0.89	−0.78	−0.63	−0.97	−0.86	−0.71

determined at −600 mV, has been solved at 1.03 Å in the presence of HCO_3^-/CO.[19] Since the latter structure was not yet available when we started our study on Ni-CODH, the first structure was used as the starting geometry of the C-cluster for DFT calculations.

Notably, geometry optimization of the large model $LM^{H+,K+}$ of μCO_2 in the C_{red2} state does not lead to a significant structural rearrangement of the C-cluster (see Figure 2a and Table S7). However, the optimized structure differs from the starting structure in the position and in the geometry of the bound CO_2 molecule. The predicted Ni−C distance (1.86 Å) is shorter than that found in the 3B52 structure (1.96 Å), whereas the C−O1 (hereafter, O1 refers to the carboxyl oxygen atom of CO_2 bound to Fe_u) distance (1.32 Å) is longer than the corresponding experimental value (1.25 Å). In the optimized structure the bound CO_2 molecule is also slightly more bent; the O1−C−O2 angle (hereafter, the O2 label refers to the nonbridging oxygen atom) of 122.2° is about 10° smaller than in the 3B52 structure (132.6°). Nevertheless, it should be noted that the geometry of CO_2 predicted by our calculations is very similar to that found in the true atomic resolution 4UDX structure. In the latter, the Ni−C bond (1.81 Å) is substantially shorter than that determined earlier (1.96 Å), whereas the two C−O bonds are considerably elongated (C−O1 and C−O2 distances are 1.32 and 1.30 Å, respectively). The O1−C−O2 angle (117.2°) is instead 15° smaller than that estimated in the 3B52 structure. All of these values are better reproduced by our calculations. In addition, the predicted distances between the CO_2 oxygen atoms and the H-bonded nitrogen atoms of His93 and Lys563 are in better agreement with those found in the 4UDX structure. Indeed, the computed O1−N(Lys563) and O2−εN(His93) distances are 2.82 and 2.56 Å, whereas they are equal to 2.72 and 2.70 Å in the 4UDX structure.

It is interesting to note that no significant structural differences have been found in the CO_2 geometry of the CO_2-bound C-cluster in C_{int} and C_{red1}, with respect to the C_{red2} state. On the other hand, substantial geometry changes have been determined for the $[NiFe_4S_4]$ cluster and for the side chain of the Cys526 residue (see Table S7). In particular, oxidation of C_{red2} to C_{int} and then to C_{red1} leads to the progressive contraction of the C-cluster with the sulfur atom of Cys526 approaching the Fe_u ion, as indicated by the Ni−S_4 and Fe_u−S(Cys526) distances respectively equal to 3.59 and 3.48 Å in C_{red2}, 3.53 and 3.38 Å in C_{int}, and 3.27 and 2.65 Å in C_{red1}.

In order to evaluate the effect of the protonation state of the His93 and the Lys563 residues on the bonding mode of CO_2 to the active site, we have also considered μ-CO_2-bound large models in which His93 and Lys563 are modeled as neutral residues ($LM^{H0,K+}$ and $LM^{H+,K0}$ large-size models, respectively), as well as the SM small-size model in which such residues are not considered at all (see Figure 2b−d). We found that the geometry of CO_2 as well as of the $[NiFe_4S_4]$ cluster is only slightly affected by the second coordination sphere. On the other hand, the comparison of the crystallographic O2−εN_{His93}, O1−εN_{His93} and O1−εN_{Lys563} distances with those predicted using the $LM^{H+,K+}$, $LM^{H0,K+}$, and $LM^{H+,K0}$ large models (see Table S7) clearly suggests that in 3B52 and 4UDX His93 and Lys563 are both positively charged. Indeed, these distances are well reproduced in the $\boldsymbol{\mu CO_2\text{-}LM^{H+,K+}}$ species, whereas εN_{His93}−O1 and εN_{His93}−O2 distances in $\boldsymbol{\mu CO_2\text{-}LM^{H0,K+}}$ and the O1−N_{Lys563} distance in $\boldsymbol{\mu CO_2\text{-}LM^{H+,K0}}$ are much larger than those found in the two crystal structures. The increase in such distances is the direct consequence of the repulsive interaction between the electron density of the CO_2 oxygen atoms and either the lone pair of εN_{His93} in $\boldsymbol{\mu CO_2\text{-}LM^{H0,K+}}$ or that of εN_{Lys563} in $\boldsymbol{\mu CO_2\text{-}LM^{H+,K0}}$. The movement of neutral His93 and Lys563 away from the CO_2 ligand leads to a slight rearrangement of the residues directly H bonded to them: namely, Asp219 and Gln332. No appreciable differences are instead predicted in the geometry of other residues. Superimposition of the geometries of the C_{red2}-μCO_2 species optimized with the $LM^{H+,K+}$, $LM^{H0,K+}$, and $LM^{H+,K0}$ models clearly show such effects (see Figure S1a). A large distortion for the $[NiFe_4S_4]$ cluster has been instead observed when the small model is used (see Figure 2d). For the large models, oxidation of the μ-CO_2-bound C-cluster leads to a progressive contraction of the $[NiFe_4S_4]$ cluster and the movement of Cys526 toward Fe_u, but the Ni−S4 and Fe_u−S(Cys526) distances predicted with the SM model are significantly shorter than those calculated using the large models and those of the X-ray structures.

The validity of our DFT models for the prediction of the geometry of the Ni-CODH active site has been checked by calculating the root-mean-square deviation (RMSD) values of the $[NiFe_4S_4]$-CO_2 cluster extracted by theoretical and experimental geometries (see Table S8). The RMSDs calculated using the large models of the active site are significantly lower than those computed using the small model, confirming the key role of the protein environment in tuning the geometry of the active site and justifying the large size of the model used in this work. Furthermore, it should be noted that the RMSD values between the DFT models of the μ-CO_2-bound C-cluster and the true atomic resolution 4UDX crystal structure are generally smaller than those computed with respect to the lower resolution 3B52 X-ray structure, despite the fact that the latter has been used as the starting geometry for our DFT calculations.

A comparison of the RMSDs calculated for the $[NiFe_4S_4]$ core and the CO_2 ligand separately confirms that, as discussed above, the protein environment mainly affects the geometry of the metallic cluster rather than the geometry of the bound CO_2. The very similar RMSD values for $LM^{H+,K+}$, $LM^{H0,K+}$, and $LM^{H+,K0}$ show instead that the protonation state of His93 and Lys563 does not affect the geometry of the $[NiFe_4S_4]$-CO_2 cluster (see Table S8). On the other hand, RMSDs calculated also including the side chains and the Cα atoms of His93 and Lys563 clearly show that in the 4UDX X-ray structure His93 and Lys563 are both positively charged; the RMSD for $LM^{H+,K+}$ is significantly

https://dx.doi.org/10.1021/acs.inorgchem.0c03034
Inorg. Chem. 2021, 60, 387−402

Table 2. Binding Energies (in kcal/mol) of CO_2 to the C-Cluster and the OH-Bound C-Cluster ($\Delta E(\mu CO_2)$, $\Delta E(tCO_2)$, and $\Delta E(CO_2\text{-}OH)$) and Relative Stabilities of μCO_2 and tCO_2 ($\Delta E(\mu CO_2) \rightarrow \Delta E(tCO_2)$), Computed Using the $LM^{H+,K+}$, $LM^{H0,K+}$, $LM^{H+,K0}$, and SM Models of the Active Site

	$\Delta E(\mu CO_2)$			$\Delta E(tCO_2)$			$\Delta E(\mu CO_2 \rightarrow tCO_2)$			$\Delta E(CO_2\text{-}OH)$		
	C_{red2}	C_{int}	C_{red1}	C_{red2}	C_{int}	C_{red1}	C_{red2}	C_{int}	C_{red1}	C_{red2}	C_{int}	C_{red1}
$LM^{H+,K+}$	−35.4	−19.5	−8.3	−24.5	−8.8		+10.9	+10.7		+4.7[a]	+8.9[a]	+5.3
$LM^{H0,K+}$	−19.6	−4.7	+11.4	−3.3	+3.5	+13.1	+16.3	+8.2	+1.7	+5.4[a]	+17.1[a]	+21.1
$LM^{H+,K0}$	−34.8	−17.5	−2.6							+19.4[a]	+24.5[a]	+25.8
SM	−8.4	+1.4	+6.4	−13.3	−2.9	+4.9	−4.9	−4.3	−1.5	−19.6	−14.4	−5.0

[a]Energy values also involve the reaction energy associated with the deprotonation of H_2O by His93 or Lys563 and migration of the resulting hydroxide to the Fe_u site.

lower than those of $LM^{H0,K+}$ and $LM^{H+,K0}$ (see Figure S2). Calculations of RMSD values among the structures of C_{red2}-μCO_2 optimized with the $LM^{H+,K+}$, $LM^{H0,K+}$, and $LM^{H+,K0}$ models including all the (non-hydrogen) atoms of the models confirm instead that the greater difference among such models is the geometry of His93 and Lys563. Indeed, despite the greater number of atoms involved in the calculation, they are smaller than or very similar to those calculated only on the CO_2-bound C-cluster and the His93 and Lys563 residues (see Table S9). Finally, the RMSD value computed for the $LM^{H+,K+}$ CO_2-bound C-cluster in the C_{red2} state is lower than that calculated for the C_{red1} state, supporting the assignment of the 3B52 and 4UDX structures to the C_{red2} state (see Table S8).

The bent geometry of the bound CO_2 molecule and the elongation of both C−O bonds is a clear manifestation of the reductive activation of CO_2. An electron transfer from the C-cluster to the CO_2 ligand is confirmed by the partial NBO charge of the bound CO_2 (see Table 1). In the $\boldsymbol{\mu CO_2\text{-}LM^{H+,K+}}$ species, the charges of CO_2 in the C_{red2}, C_{int}, and C_{red1} states are equal to −1.03, −0.98, and −0.91, respectively. The decrease in the CO_2 negative charge in species in which His93 and Lys563 are deprotonated ($LM^{H0,K+}$ and $LM^{H+,K0}$) or absent (SM model) highlights the effect of the protonation state of these residues in the electron transfer from the C-cluster to CO_2.

An analysis of the CO_2 Mulliken spin population, which is always equal to zero (see Table S10), allows us to rule out the reduction of CO_2 to the $CO_2^{\bullet-}$ radical and strongly suggests a bielectronic reduction to the formal diamagnetic CO_2^{2-} species, as also indicated by previous calculations.[20] Such a bielectronic reduction is also indicated by the geometry parameters of the bound CO_2. Indeed, the C−O bond lengths and the O1−C−O2 angle of the CO_2 ligand coordinated to the large models of the C-cluster best match those of CO_2^{2-} (1.32 Å and 118°, respectively). The CO_2 charge of about −1, lower than the expected value of −2, can be attributed to the large charge delocalization provided by the covalent linkage between CO_2 and the metal sites.

The reductive activation of CO_2 corresponds to the oxidation of the C-cluster. A detailed analysis of the electronic structure of CO_2-bound and unbound species allowed us to identify the metal sites that are mainly involved in the oxidation. In this respect, due to the well-known electron spin and charge delocalization in FeS clusters, an analysis of the electronic structure of the C-cluster can be still more insightful, considering the net charges of the two subunits $\{Fe_1NiFe_uS_1S_2\}$ (hereafter labeled layer L1) and $\{Fe_3Fe_4S_3S_4\}$ (hereafter labeled layer L2). L1 and L2 correspond respectively to the blue and red layers of the BS coupling schemes shown in Scheme S1. A comparison of the electronic structure of the $\boldsymbol{C_{red2}\text{-}\mu CO_2\text{-}LM^{H+,K+}}$ model, corresponding to X-ray structures of the CO_2-bound C-cluster,[5,19] and the unbound form of the C-cluster in the same redox state, $\boldsymbol{C_{red2}\text{-}LM^{H+,K+}}$, indicates that the oxidation of the C-cluster occurs predominantly on the L1 layer. Indeed, the charge of the L1 layer in $\boldsymbol{C_{red2}\text{-}\mu CO_2\text{-}LM^{H+,K+}}$ is 0.69 more positive than that in $\boldsymbol{C_{red2}\text{-}LM^{H+,K+}}$. In particular, the atomic charge of Fe_u is significantly affected by the CO_2 binding; in $\boldsymbol{C_{red2}\text{-}\mu CO_2\text{-}LM^{H+,K+}}$ it is 0.18 more positive than that in $\boldsymbol{C_{red2}\text{-}LM^{H+,K+}}$ (see Table S11). Conversely, atomic charges on Ni and other Fe atoms do not differ by more than 0.05. These results suggest that the CO_2 binding to the C_{red2} state of the C-cluster promotes an electron transfer from the Fe_u-containing layer to the CO_2 ligand. Analogously, also in $\boldsymbol{C_{int}\text{-}\mu CO_2\text{-}LM^{H+,K+}}$ and $\boldsymbol{C_{red1}\text{-}\mu CO_2\text{-}LM^{H+,K+}}$ the CO_2 ligand is reduced mainly at the expense of the L1 layer of the C-cluster, and in particular of the Fe_u atom. A similar electronic structure is observed with the $LM^{H0,K+}$, $LM^{H+,K0}$, and SM models (see Table S11).

The effect of the CO_2 binding on the electronic structure of the C-cluster is also evidenced by an inspection of the frontier orbitals of unbound and CO_2-bound adducts of the C-cluster. In all redox states, indeed, binding of CO_2 leads to a significant stabilization of both the HOMO and LUMO levels (see Table S12). The stabilization of the HOMO and LUMO indicates that, after the binding of CO_2, the C-cluster is simultaneously more difficult to oxidize and easier to reduce. To confirm such a finding, energy differences between reduced and oxidized species ($E_{red} - E_{ox}$) have been calculated for μCO_2 adducts and unbound forms of the C-cluster. Such values are expected to provide an estimate of the propensity of an oxidized species to be reduced and, therefore, to follow the same trend of the experimental reduction potentials; the more negative the $E_{red} - E_{ox}$ value (the more positive the potential), the greater its tendency to be reduced. Notably, $E_{red} - E_{ox}$ values for μCO_2 adducts are at least 0.5 eV lower than those calculated for the unbound forms of the C-cluster (see Table S13). For instance, in the reduction from C_{red1} to C_{int} the $E_{red} - E_{ox}$ values for unbound and CO_2-bound $LM^{H+,K+}$ models are respectively −1.43 and −1.92 eV, whereas in the reduction from C_{int} to C_{red2} they are +0.09 and −0.60 eV. These results clearly indicate that the binding of CO_2 to the C-cluster promotes the reduction of the active site. This is consistent with electron transfer from the cluster to the CO_2 ligand.

Finally, to understand how the protein environment and the redox state of the C-cluster tune the reactivity of the active site, the binding energies of CO_2 in the C_{red2}, C_{int}, and C_{red1} states have been evaluated using the different models of the active site (see Table 2). Binding of CO_2 in the μ_2-η^2(C,O) mode to the SM model is exoergic only in the case of the C_{red2} state (−8.4 kcal/mol), whereas it turns out to be endoergic by 1.4 and 6.4 kcal/mol for C_{int} and C_{red1}, respectively. On the other hand, binding of CO_2 to the $LM^{H+,K+}$ model is always calculated to be

https://dx.doi.org/10.1021/acs.inorgchem.0c03034
Inorg. Chem. 2021, 60, 387−402

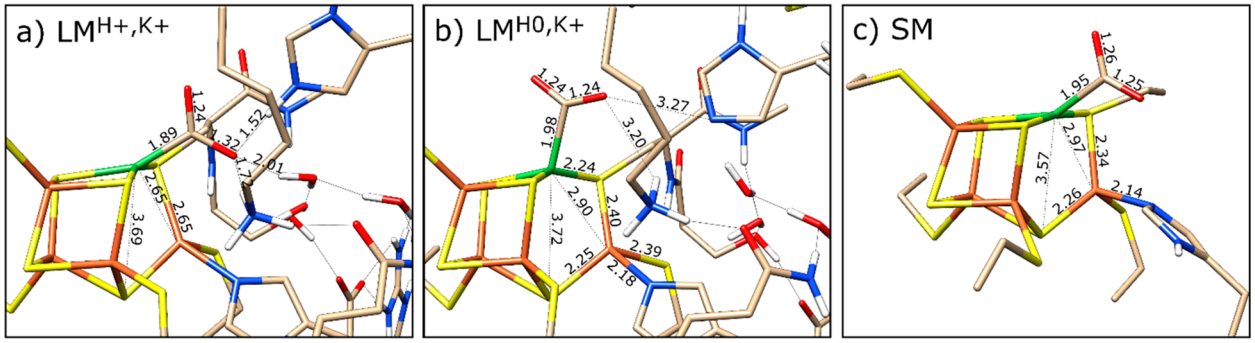

Figure 3. Schematic representation of the geometries of the tCO_2-bound form of the C-cluster in the C_{red2} state optimized using the (a) $LM^{H+,K+}$, (b) $LM^{H0,K+}$ and (c) SM models. Selected interatomic distances are given in Å. For the sake of clarity, aliphatic hydrogen atoms are not shown.

energetically favored, with CO_2 binding energies becoming less negative with the oxidation of the C-cluster from C_{red2} (−35.4 kcal/mol) to C_{int} (−19.5 kcal/mol) and to C_{red1} (−8.3 kcal/mol). The large difference between the binding energies calculated for the SM model and those calculated for the $LM^{H+,K+}$ model highlights the fundamental role of the protein environment in tuning the stability of the μCO_2-bound forms of the enzyme. The interaction of CO_2 with the C-cluster is critically assisted by the network of H bonds formed near the active site. In particular, His93 and Lys563 may be crucial for the CO_2 coordination. The elongation of H-bond distances between these residues and the oxygen atoms of CO_2 with the oxidation of the active site from C_{red2} to C_{red1} (see Table S7) reflects the smaller stabilization of the CO_2-bound adduct by the protein environment.

Notably, deprotonation at the εN atom of His93 ($LM^{H0,K+}$ model) induces an unfavorable interaction between that atom and the O2 atom of CO_2. This makes the binding of CO_2 a less favorable process; in C_{red2} and C_{int} it is still favored by 19.6 and 4.7 kcal/mol, respectively, whereas in the C_{red1} redox state it turns out to be endoergic by 11.4 kcal/mol (even more endoergic than that computed with the SM model). On the other hand, the protonation state of Lys563 only slightly affects the CO_2 binding, as indicated by the similar binding energies calculated for the $LM^{H+,K+}$ and the $LM^{H+,K0}$ models. The main stabilizing interaction in μCO_2 adducts is therefore the H bond between the hydrogen atom bound to the εN atom of His93 and the O2 oxygen atom of CO_2. Accordingly, the $\boldsymbol{\mu CO_2\text{-}LM^{H+,K0}}$ species have been always calculated to be more stable than the $\boldsymbol{\mu CO_2\text{-}LM^{H0,K+}}$ isomers by more than 8 kcal/mol. On the basis of these results it is also possible to suggest that the His93 residue, depending on its protonation state, may favor the binding or the release of the CO_2 molecule from the C-cluster. CO_2 can bind to the active site when His93 is doubly protonated, where the formation of two strong H bonds promotes the CO_2 coordination. CO_2 may be released instead when the histidine residue is deprotonated on εN. This conclusion is based on the plausibility of different protonation states for His93 during catalysis; this residue was in fact proposed to be involved in proton transfer from/to the C-cluster.[25,26]

Terminal Binding of CO_2 to the Ni Atom of the C-Cluster. All species in which CO_2 is terminally bound to Ni or Fe_u by one oxygen atom are unstable, resulting in CO_2 release from the active site or isomerization to the more stable structure in which CO_2 bridges the Ni-Fe_u site (μCO_2 species) during geometry optimization. Conversely, species in which the CO_2 ligand is terminally bound to the Ni ion through the carbon atom (tCO_2 species) have been generally identified as stable isomers (see Figure 3). When calculations are carried out using the SM model, the tCO_2 species are even more stable than the corresponding μCO_2 isomers by about 5, 4, and 2 kcal/mol in the C_{red2}, C_{int}, and C_{red1} states, respectively. Notably, the relative stability is reversed in the case of the LM models, pointing out the effect of the protein environment in modulating the stability of the two isomers. The lower stability of tCO_2 with respect to μCO_2, due to the lower interaction between the oxygen atoms of CO_2 and the nearby residues (see Figures 2a,b and 3a,b), is in agreement with the fact that only the bridging CO_2 species has been characterized by X-ray studies.[5,19]

When both His93 and Lys563 are positively charged ($LM^{H+,K+}$ model), tCO_2 is a stable species only in the C_{red2} and C_{int} redox states. Even though both C_{red2}-tCO_2 and C_{int}-tCO_2 are less stable than the corresponding μCO_2 isomers by about 11 kcal/mol, binding of CO_2 is still energetically favored by 24.5 and 8.8 kcal/mol, respectively. This result supports the hypothesis that the tCO_2 species corresponds to a catalytic intermediate in which a first covalent interaction is established between CO_2 and the metallic cluster. Notably, deprotonation of His93 ($LM^{H0,K+}$ model) strongly affects the binding energies of tCO_2 (as already observed for μCO_2), as well as the relative stability of the tCO_2 vs μCO_2 isomers. tCO_2 binding energies are equal to −3.3, 3.5, and 13.1 kcal/mol for the C_{red2}, C_{int}, and C_{red1} states, respectively. This results in the tCO_2 isomer being less stable than the μCO_2 isomer by as much as 16.3 kcal/mol in the C_{red2} state, whereas the energy difference decreases by about 2 kcal/mol in the C_{red1} form (see Table 2). Conversely, deprotonation of Lys563 ($LM^{H+,K0}$ model) did not allow for the identification of the tCO_2 adduct as a genuine energy minimum on the PES, for all of the redox states considered, since during geometry optimizations they isomerized to the μCO_2-$LM^{H+,K0}$ or the tCO_2-$LM^{H0,K+}$ species.

In addition, the geometries of the tCO_2 adducts are significantly affected by the protonation state of His93. When both His93 and Lys563 are protonated, the Ni atom retains a square-planar arrangement of ligands, even if it is slightly more distorted than that observed in μCO_2, whereas when His93 is neutral, the Ni atom adopts a distorted-tetrahedral geometry (see Figure 3 and Table S14). The difference in the Ni geometries can be attributed to the different interactions established by CO_2 with the protein surroundings. In the $\boldsymbol{tCO_2\text{-}LM^{H+,K+}}$ species, the square-planar coordination of Ni is favored by the strong H-bond interactions between the O1 oxygen atom of CO_2 and the positively charged His93 and Lys563. On the other hand, deprotonation of His93 generates a repulsive interaction that moves the lone-pair electrons of the

https://dx.doi.org/10.1021/acs.inorgchem.0c03034
Inorg. Chem. 2021, 60, 387−402

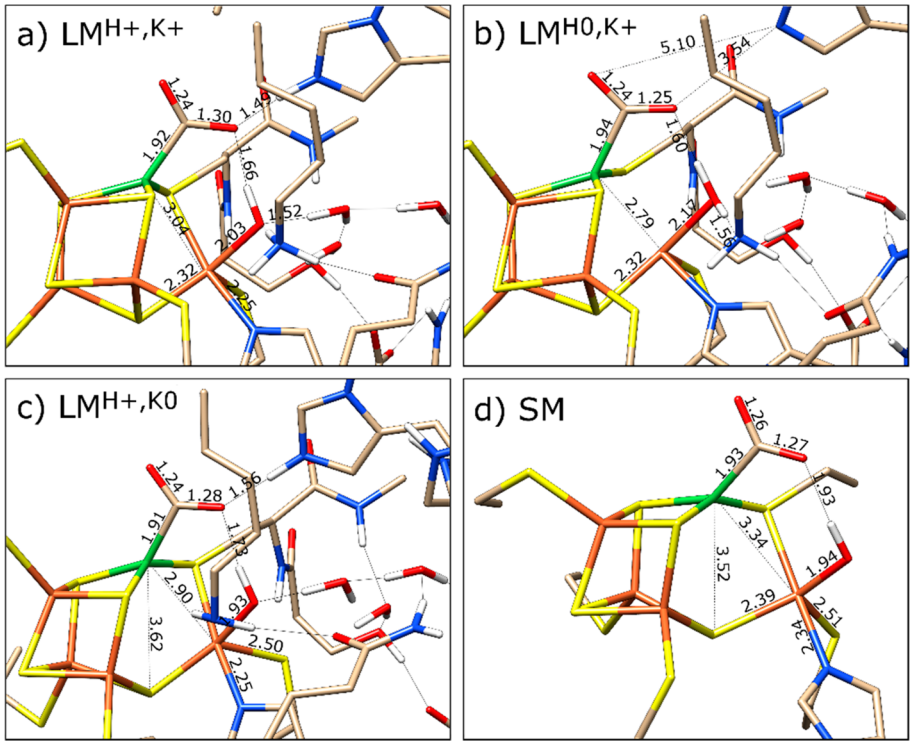

Figure 4. Schematic representation of the geometries of the CO_2-OH-bound form of the C-cluster in the C_{red2} state optimized using the (a) $LM^{H+,K+}$, (b) $LM^{H0,K+}$, (c) $LM^{H+,K0}$, and (d) SM models. Selected interatomic distances are given in Å. Aliphatic hydrogen atoms are not shown.

O1 oxygen atom far away from the neutral N atom of His93 and therefore pushes the CO_2 ligand to a more apical position. The rearrangement of CO_2 and His93, due to the deprotonation of the histidine residue (see Figure S1b) results in large RMSD values between the **tCO_2-$LM^{H+,K+}$** and **tCO_2-$LM^{H0,K+}$** adducts (see Table S9).

In the tCO_2 species, as observed for the μCO_2 isomers, the bound CO_2 molecule features a large negative charge, and the charge is transferred from the Fe_u-containing layer (see Table 1 and Table S11). Interestingly, when His93 is doubly protonated, such a negative charge is very similar to that computed for the μCO_2 isomers, indicating a formal reduction of CO_2 to a carboxylate anion, whereas when His93 is singly protonated, the negative charge of CO_2 is significantly smaller. In fact, the charges are −0.95 and −0.88 in **C_{red2}-μCO_2-$LM^{H+,K+}$** and **C_{int}-μCO_2-$LM^{H+,K+}$**, respectively, whereas they are −0.73 and −0.56 in **C_{red2}-tCO_2-$LM^{H0,K+}$** and **C_{int}-tCO_2-$LM^{H0,K+}$**, respectively. Deprotonation of His93 therefore promotes an electron transfer from CO_2 to the C-cluster, possibly decreasing its tendency to be reduced and simultaneously increasing its tendency to be oxidized. A comparison of HOMO and LUMO energies in μCO_2 and tCO_2 species and calculation of the $E_{red} - E_{ox}$ values (see Tables S12 and S13) confirm this picture. When His93 is doubly protonated, HOMO and LUMO energies in tCO_2 and μCO_2 do not differ by more than 0.05 eV. Analogously, $E_{red} - E_{ox}$ values are almost identical (−0.60 eV for μCO_2 and −0.59 eV for tCO_2 in the reduction from C_{int} to C_{red2}). On the other hand, when His93 is singly protonated, the HOMO and LUMO in tCO_2 are higher in energy than those in μCO_2 by respectively 0.24 and 0.28 eV in C_{red2}, 0.36 and 0.33 eV in C_{int}, and 0.58 and 0.27 eV in C_{red1}. Accordingly, the $E_{red} - E_{ox}$ value of the tCO_2 adduct is less negative than that of μCO_2 by 0.35 eV in the reduction from C_{red1} to C_{int} and by 0.28 eV in the reduction from C_{int} to C_{red2}. This different trend highlights the effect of the protonation state of His93 on the electronic structure of the C-cluster. When such a residue is doubly protonated, the tCO_2 and μCO_2 adducts have similar reduction and oxidation potentials, whereas when it is singly protonated, tCO_2 adducts are more difficult to reduce and easier to oxidize in comparison to the μCO_2 isomers.

It is also worth noting that, as observed for the μCO_2 adducts, the energies of frontier orbitals and $E_{red} - E_{ox}$ values of tCO_2 adducts are always more negative than those of the unbound forms of the C-cluster (see Tables S12 and S13). CO_2 binding therefore promotes the reduction of the active site independently from the coordination mode of CO_2 and the protonation state of His93. However, only when His93 is singly protonated, the isomerization from the tCO_2 to the μCO_2 adduct further promotes the reduction of the cluster. In this case, $E_{red} - E_{ox}$ energy differences calculated for μCO_2 adducts are more negative (i.e., the reduction potentials are more positive) than those computed for tCO_2 species. Consequently, the reduction of μCO_2 requires potentials less negative than those needed for the reduction of tCO_2.

Binding of CO_2 to the Ni Atom of the OH-Bound Form of the C-Cluster. The binding of CO_2 to the Ni atom of the C-cluster in which a hydroxide is terminally bound to the Fe_u atom is finally investigated. The resulting adducts, hereafter called CO_2-OH, are stable complexes in all redox states, using both large and small models (see Figure 4 and Figure S1 and Table S15). The binding mode of CO_2 is very similar to that observed for the *n*-butyl isocyanate inhibitor in the 2YIV X-ray structure,[21] with the Ni atom featuring a distorted-tetrahedral coordination, which is in contrast with the square-planar geometry observed in the μCO_2-bound C-cluster. In CO_2-OH species optimized using the $LM^{H+,K+}$ model, one oxygen atom of CO_2 forms H bonds with His93 and the OH^- ligand coordinated to Fe_u, which in turn is strongly H bonded to

https://dx.doi.org/10.1021/acs.inorgchem.0c03034
Inorg. Chem. 2021, 60, 387−402

Lys563 (see Figure 4a). In species optimized using the $LM^{H0,K+}$ and SM models in which the His93 residue is deprotonated at the εN atom (see Figure 4b) or absent (see Figure 4d), the same oxygen atom of CO_2 only interacts with the hydroxide ligand bound to Fe_u. On the other hand, the H bond with Lys563 is lost in the CO_2-OH adducts optimized with the SM and $LM^{H+,K0}$ models (see Figure 4c,d). It is interesting to note that during the geometry optimization of $\mathbf{C_{red2}}$-$\mathbf{CO_2}$-OH-$\mathbf{LM^{H0,K+}}$ a proton of Lys563 is transferred to the hydroxide ligand, leading to the formation of a water molecule still bound to Fe_u (Fe_u-O_{OH2} and $H_{OH2}-N_{Lys563}$ distances equal to 2.17 and 1.56 Å, respectively).

In order to calculate the binding energies of CO_2 in the CO_2-OH adducts, the OH-bound forms of the C-cluster have been characterized. In the case of the SM model, for which no second-sphere residues are included, a stable species with the OH^- ligand terminally coordinated to Fe_u has been identified for all of the redox states investigated (C_{red1}, C_{int}, C_{red2}). Binding of CO_2 to such species is always an exoergic process, being equal to about −20 kcal/mol in the C_{red2} state and decreasing to about −5 kcal/mol in the C_{red1} state (see Table 2). Nevertheless, the results are very different when second-sphere residues are included in the LM models. In the C_{red1} state the hydroxide ligand is still terminally coordinated to the Fe_u site, completing its distorted-tetrahedral geometry in accord with the crystal structures of *C. hydrogenoformans* CODH[5] and *M. thermoacetica* CODH/ACS[53] (structures 3B53/3B51 and 3I01, respectively). On the other hand, in C_{int} and C_{red2} the OH^- ligand is protonated to H_2O that dissociates from the C-cluster. In particular, in the $LM^{H+,K+}$ model, the proton is transferred from His93 and the dissociation of water is favored by the formation of a strong H-bond network with Lys563, His93, and a conserved water molecule, whereas in the case of the $LM^{H0,K+}$ model the proton is transferred from Lys563, and the formed water molecule remains weakly bound to Fe_u (the Fe_u-OH_2 distance is equal to 2.24 and 2.42 Å in C_{int} and C_{red2}, respectively). Interestingly, the OH-bound forms of the C-cluster optimized using the $LM^{H+,K0}$ model converge to those optimized with the $LM^{H0,K+}$ model through the transfer of the εN proton from His93 to the OH^- ligand.

According to the results presented above for the LM models, only the C_{red1} state is compatible with the OH-bound form of the C-cluster, since in the C_{int} and C_{red2} states the hydroxide ligand dissociates as a water molecule. The absence of the hydroxide ligand in the C_{red2} state is supported by spectroscopic experiments; the loss in C_{red2} of the strong ENDOR signal observed for the C_{red1} state was indeed attributed to the release of OH^-.[54] Furthermore, Fontecilla-Camps et al.[14] noticed that the X-ray structures, featuring a nonbridging hydroxide ligand bound to the Fe_u atom, solved at −320 mV (3B53) and −600 mV (3B51) that have been previously assigned to the C_{red1} and C_{red2} states, respectively, are almost identical, suggesting that the latter is a mixture of the C_{red1} state (3B53) and the CO_2 adduct of the C-cluster in the C_{red2} state (3B52).

Since the OH-bound form of the enzyme in the C_{red2} and C_{int} states is unstable, binding of CO_2 to the OH-bound C-cluster can be considered only for the C_{red1} state for which, in contrast to the SM model, is always an endoergic process (+5.3, +21.1, and +25.8 kcal/mol for the $LM^{H+,K+}$, $LM^{H0,K+}$, and $LM^{H+,K0}$ models, respectively). Instead, for C_{int} and C_{red2}, we can calculate the ΔE value associated with the formation of the CO_2-OH adduct by the simultaneous binding of CO_2 and OH^- (see values indicated by footnote *a* in Table 2 and Scheme S2), according to the reactions represented in Scheme 2A. In this

Scheme 2. Possible Mechanisms for the Formation of (a) C_{red2}-CO_2-OH-$LM^{H+,K+}$, (b) C_{int}-CO_2-OH-$LM^{H+,K+}$, and (c) C_{red1}-CO_2-OH-$LM^{H+,K+}$

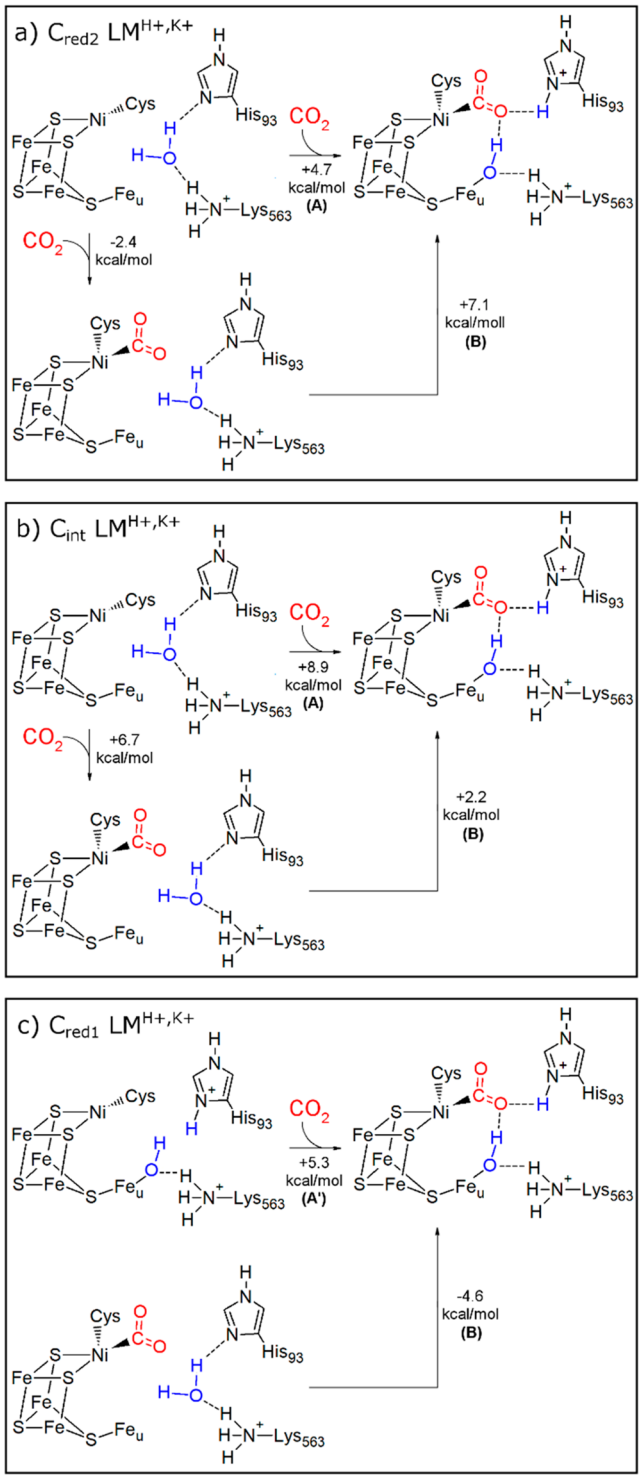

case as well, the formation of the CO_2-OH adducts is predicted to be an endoergic process for all of the protonation states investigated; even if the CO_2-OH adducts are genuine minima on the PES, they are unstable with respect to the release of the CO_2 and H_2O substrates. However, the CO_2-OH species may still be intermediates along the CO_2 binding/dissociation pathways (see below). In this respect, it is also interesting to evaluate the ΔE value associated with the deprotonation of a

https://dx.doi.org/10.1021/acs.inorgchem.0c03034
Inorg. Chem. 2021, 60, 387−402

Scheme 3. Schematic Representation of CO_2 Binding to the CODH Active Site[a]

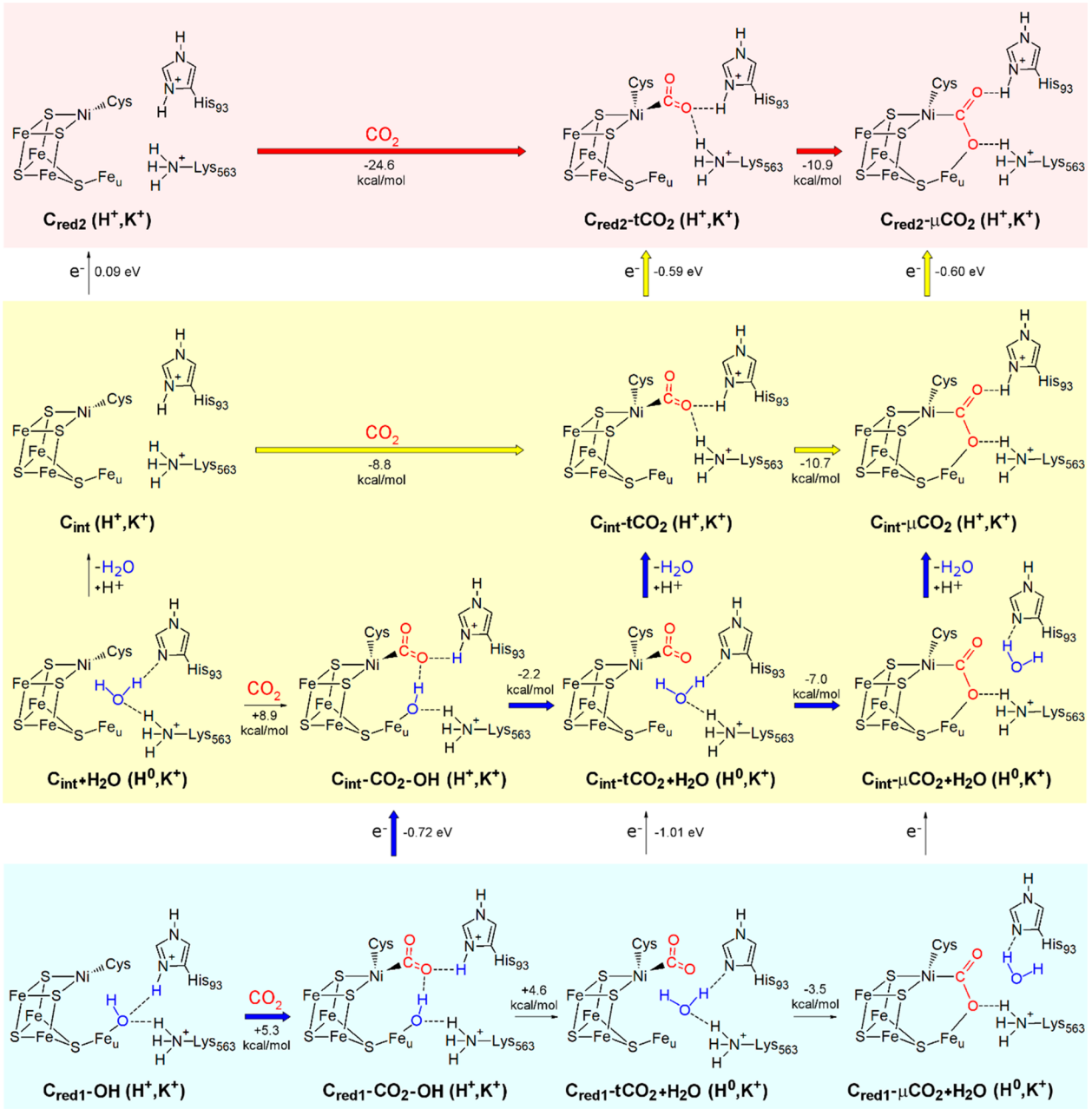

[a]In C_{red2} and C_{int}, CO_2 initially binds to the terminal position of the Ni atom of the unbound C-cluster. Subsequent isomerization yields the more stable μCO_2 species (see red and yellow arrows). In C_{red1}, CO_2 binds to the OH-bound C-cluster. Reduction and H_2O release are required for the formation of μCO_2 (see blue arrows). Red, yellow, and cyan backgrounds denote species in C_{red2}, C_{int}, and C_{red1}, respectively.

water molecule and coordination of the resulting hydroxyl ligand to Fe_u in the tCO_2 forms of the enzyme to give the CO_2-OH adducts, according to the reactions in Scheme 2B. Such a process calculated for the $LM^{H+,K+}$ model is endoergic by 7.1 and 2.2 kcal/mol in the C_{red2} and C_{int} states, respectively, whereas it turns out to be exoergic by about 5 kcal/mol in the case of C_{red1}.

As in μCO_2 and tCO_2 species, in CO_2-OH adducts the bound CO_2 molecule features a large negative charge (see Table 1 and Table S16), indicating an electron transfer from the C-cluster to CO_2. Notably, as observed for the binding of CO_2 to the unbound C-cluster, the binding of CO_2 to the OH-bound form of the enzyme in the C_{red1} state promotes the reduction of the C-cluster and simultaneously makes its oxidation more difficult. The HOMO and LUMO in **C_{red1}-CO_2-OH** are indeed lower in energy than those in **C_{red1}-OH** by 0.42 and 0.26 eV, respectively, when His93 is doubly protonated, and by 0.39 and 0.29 eV when His93 is singly protonated (see Table S12).

DISCUSSION

In light of the results presented above it is possible to propose a mechanism for the binding and the dissociation of CO_2 to and from the C-cluster. However, such processes are differently affected by the protonation state of the surrounding residues and the redox state of the C-cluster. The two mechanisms are therefore discussed in different schemes.

https://dx.doi.org/10.1021/acs.inorgchem.0c03034
Inorg. Chem. 2021, 60, 387−402

Scheme 4. Schematic Representation of CO_2 Dissociation from the μCO_2 Adduct of the Active Site in the C_{red2} Redox State[a]

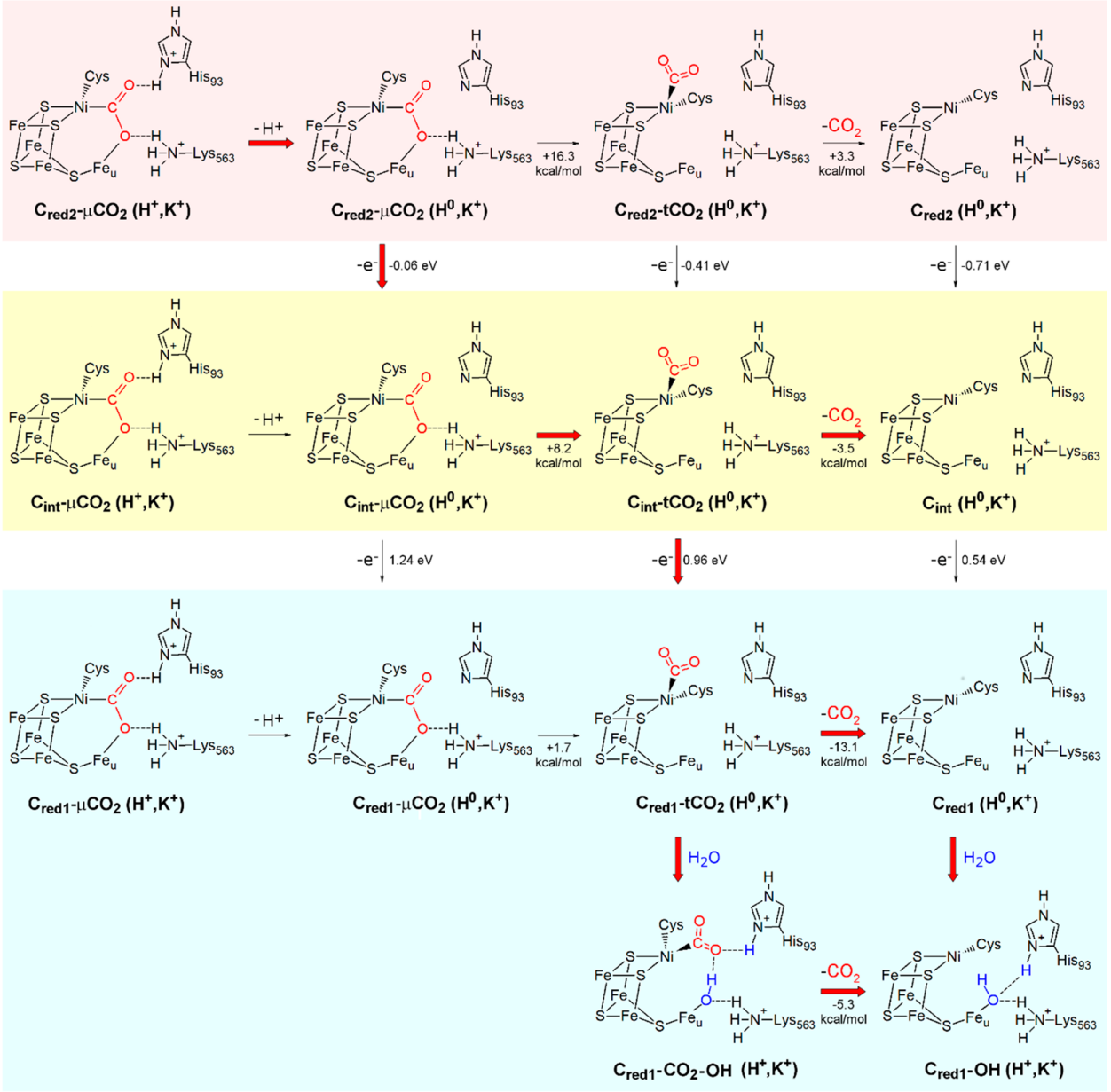

[a]The most plausible mechanisms are indicated by red arrows. Deprotonation of His93 promotes oxidation of C_{red2}-μCO_2 to C_{int}-μCO_2. The latter isomerizes to C_{int}-tCO_2, from which CO_2 can dissociate. C_{int}-tCO_2 can also be oxidized to C_{red1}-tCO_2, from which CO_2 dissociation is more favorable. Species in the C_{red2}, C_{int}, and C_{red1} redox states are denoted by red, yellow, and cyan backgrounds, respectively.

Our calculations strongly suggest that the binding of CO_2 to the C-cluster is energetically more favored when both His93 and Lys563 are in their positively charged form. Protonated His93 and Lys563, apart from stabilizing the resulting CO_2 adduct through their interaction with the oxygen atoms of bound CO_2, can also act as proton donors, as in the direction of the CO_2 reduction (i.e., in the direction of CO_2 binding) two protons have to be supplied to the active site. Our calculations, according to experimental data,[55] also indicate that CO_2 binds preferentially to the C_{red2} state of the C-cluster. C_{red2} is indeed the redox state of the active site, which always features the highest affinity for CO_2. In this state, binding of CO_2 occurs according to a dissociative mechanism (i.e., CO_2 binds to the unbound form of the C-cluster, after the release of possible other ligands). The associative mechanism (i.e., binding of CO_2 to the OH-bound form of the C-cluster) is ruled out by the incompatibility of the C_{red2} state with the OH-bound form of the C-cluster.

CO_2 approaches therefore the active site in the C_{red2} state via a hydrophobic tunnel apical to the Ni atom and initially binds to the terminal position of the Ni ion (−24.5 kcal/mol), where initial favorable interactions with protonated His93 and Lys563 are possible (see Scheme 3). Once the **C_{red2}-tCO_2 (H^+,K^+)** intermediate is formed, it easily isomerizes to the more stable μCO_2 adduct, which is strongly stabilized by the H-bond network with His93, Lys563, and a conserved water molecule (−10.9 kcal/mol). These two chemical steps are significantly less favored if the active site is oxidized to C_{int} or C_{red1}. However, binding of CO_2 to the C_{int} redox state and subsequent isomerization to the μCO_2 adduct are still energetically favored

https://dx.doi.org/10.1021/acs.inorgchem.0c03034
Inorg. Chem. 2021, 60, 387−402

by 8.8 and 10.7 kcal/mol, respectively. Nevertheless, the formation of $\mathbf{C_{int}}$-$\boldsymbol{\mu}\mathbf{CO_2}$ $(\mathbf{H^+},\mathbf{K^+})$ can be preceded by the reduction of $\mathbf{C_{int}}$-$\mathbf{tCO_2}$ $(\mathbf{H^+},\mathbf{K^+})$ to $\mathbf{C_{red2}}$-$\mathbf{tCO_2}$ $(\mathbf{H^+},\mathbf{K^+})$. The CO_2 binding step indeed induces a transfer of electron density from the cluster to CO_2, that in turn promotes the reduction of the C-cluster, as clearly indicated by the significant decrease in the $E_{red} - E_{ox}$ value (from 0.09 eV in $\mathbf{C_{int}}$ $(\mathbf{H^+},\mathbf{K^+})$ to −0.59 eV in $\mathbf{C_{int}}$-$\mathbf{tCO_2}$ $(\mathbf{H^+},\mathbf{K^+})$; see Scheme 3).

Differently from the binding of CO_2 to the C_{red2} and the C_{int} redox states, binding of CO_2 to C_{red1} should proceed by an associative mechanism. Our calculations indeed support the experimental assignment[5,13,53,54] of C_{red1} to the OH-bound form of the C-cluster. Therefore, in this state, CO_2 should bind to the Ni atom of the C-cluster when a hydroxide ligand is still coordinated to Fe_u. Such a step is endoergic by 5.3 kcal/mol. This value, however, is not sufficiently high to exclude the possibility that CO_2 binds to C_{red1}. Accordingly, several experimental studies support the binding of CO_2 also to C_{red1}, even if CO_2 has been proposed to bind to the C_{red2} redox state. Indeed, exposure to CO_2 slightly affects the C_{red1} EPR g values,[56] whereas exposure to the CO_2 analogue and competitive inhibitor CS_2 under reducing conditions leads to the disappearance of the C_{red1} EPR signal and the slow formation of a novel signal.[1,55] Furthermore, exposing particular batches of CODH, which are unable to convert C_{red1} to C_{red2}, to CO_2/dithionite (but not dithionite itself) can "cure" such batches, allowing them to attain the C_{red2} state.[57] It is difficult to envisage that CO_2 has these effects unless it could bind to the enzyme when the C-cluster is in a state more oxidized than C_{red2}. Therefore, it has been proposed that CO_2 binds C_{red1} noncatalytically, perturbating its EPR signal but without accepting an electron pair from the enzyme.[57] The resulting species could correspond to the $\mathbf{C_{red1}}$-$\mathbf{CO_2}$-$\mathbf{OH}$ $(\mathbf{H^+},\mathbf{K^+})$ adduct. As shown in Scheme 3, conversion of such an intermediate in the μCO_2 adduct requires the transfer of a proton from His93 to the hydroxide ligand that is released from the active site as a H_2O molecule. Notably, such a step in the C_{red1} state is energetically disfavored by 4.6 kcal/mol, whereas it is slightly exoergic in the C_{int} state (−2.2 kcal/mol). This result suggests that the formation of the μCO_2 adduct (whose formation is essential for CO_2 reduction) is preceded by the reduction of the C-cluster from C_{red1} to C_{int} through the transfer of one electron from the auxiliary clusters. Studies of the dependence of CO_2 reduction by *R. rubrum* CODH on the redox state of the C-cluster support this hypothesis; C_{red1} is indeed not competent to reduce CO_2, whereas its one-electron-reduced state is active for CO_2 reduction.[58] Actually, the point that CO_2 binds more strongly to the reduced form of the C-cluster can be equivalently investigated by looking at reduction propensities: the decrease in the LUMO energy of about 0.3 eV after the binding of CO_2 (see Table S12) suggests that the CO_2-OH adduct is more easily reduced than the OH-bound form, in accordance with the experimental observation in which the reduction of the C-cluster from C_{red1} to C_{red2} is strongly speeded up by the presence of the CO_2 substrate.[57] The formation of $\mathbf{C_{int}}$-$\mathbf{tCO_2}$+$\mathbf{H_2O}$ $(\mathbf{H^+},\mathbf{K^+})$ therefore follows a CEC mechanism. Finally, the tCO_2 to μCO_2 isomerization can take place before or after further reduction of the C-cluster (see Scheme 3). Due to the rather complex picture described above for CO_2 binding, we consider it useful to summarize in a bullet point list the most likely and most intriguing routes for CO_2 binding. Such a list—included in the following—will contain most of the information coming from the colored arrows in Scheme 3, as they indicate steps that are relatively favored in the energy landscape composed by the intermediates investigated in the present contribution:

- The most likely route for CO_2 binding involves the C_{red2} state featuring both His93 and Lys563 in their protonated (charged) states, after H_2O has left the active site following completion of the previous catalytic cycle; as far as the regiochemistry of binding is concerned, CO_2 may first bind as tCO_2 and then evolve toward μCO_2.
- Intriguingly, CO_2 may also bind to C_{int}, which would be more likely when oxygenic ligands are absent from the active site and, at the same time, both His93 and Lys563 attain their charged (protonated) state.
- CO_2 could even bind to C_{red1}; however, such a possibility depends on the occurrence of specific conditions, which are somehow likely to be associated with formation of states not necessarily functional for catalysis to occur.

As discussed above, the release of CO_2 from the C-cluster does not occur at the same redox and protonation state of the CO_2 binding. Indeed, dissociation of CO_2 in the C_{red2} state when both His93 and Lys563 are protonated (i.e., conditions under which CO_2 binding is more favored) is a strongly endoergic process; the initial displacement of CO_2 from the bridging position to the terminal position on the Ni atom and the subsequent CO_2 dissociation are energetically disfavored by 10.9 and 24.5 kcal/mol, respectively.

Our calculations indicate that CO_2 release can take place by following a reaction pathway that implies deprotonation of a nearby residue and oxidation of the C-cluster. Accordingly, in the direction of CO oxidation (i.e., in the direction of CO_2 release) electrons and protons must be released from the active site. As shown in Scheme 4, after deprotonation of His93, the first step of CO_2 dissociation involving the μCO_2 to tCO_2 isomerization is predicted to be energetically disfavored by 16.3, 8.2, and only 1.7 kcal/mol in C_{red2}, C_{int}, and C_{red1}, respectively. Conversely, deprotonation of His93 makes the release of CO_2 from the tCO_2 adduct slightly endoergic in C_{red2} (+3.3 kcal/mol) and exoergic in C_{int} and C_{red1} (−3.5 and −13.1 kcal/mol, respectively). On the basis of these considerations, we assume that the CO_2 release occurs when His93 is singly protonated and the C-cluster is oxidized at least to the C_{int} redox state.

Notably, deprotonation of His93 can immediately induce the oxidation of the C-cluster from C_{red2} to C_{int}. Proton-coupled electron transfers (PCETs) are indeed very common reactions in chemistry and biology to balance the charge of the system. The energetics of the $\mathbf{C_{red2}}$-$\boldsymbol{\mu}\mathbf{CO_2}$ $(\mathbf{H^+},\mathbf{K^+})$ → $\mathbf{C_{int}}$-$\boldsymbol{\mu}\mathbf{CO_2}$ $(\mathbf{H^0},\mathbf{K^+})$ PCET oxidation is therefore calculated according to the procedure described in ref 20. In such a calculation, in which an (e^-, H^+) couple is removed from the active site, the experimental oxidation potential of −0.3 V[12] has been used and translated, by using the energy of a proton in water at pH 7, to 371.6 kcal/mol. Such a step is predicted to be energetically disfavored by 8.4 kcal/mol. This value, however, is not sufficiently high to exclude the feasibility of the PCET process. Accordingly, the μCO_2 to tCO_2 isomerization in the C_{red2} state is predicted to be strongly endoergic (+16.3 kcal/mol) and, therefore, unlikely to take place. Such a step in the C_{int} redox state is still endoergic (+8.2 kcal/mol), but much less than in C_{red2}. Hence, $\mathbf{C_{red2}}$-$\boldsymbol{\mu}\mathbf{CO_2}$ $(\mathbf{H^0},\mathbf{K^+})$ is oxidized to $\mathbf{C_{int}}$-$\boldsymbol{\mu}\mathbf{CO_2}$ $(\mathbf{H^0},\mathbf{K^+})$, which then isomerizes to $\mathbf{C_{int}}$-$\mathbf{tCO_2}$ $(\mathbf{H^0},\mathbf{K^+})$, from which CO_2 can dissociate (−3.5 kcal/mol, see Scheme 4). On the other hand, the possibility that a PCET oxidation occurs at the level of the C_{int} redox state is ruled out by the high

https://dx.doi.org/10.1021/acs.inorgchem.0c03034
Inorg. Chem. 2021, 60, 387−402

endoergicity of the process (+23.2 kcal/mol). The μCO_2 to tCO_2 isomerization can, however, promote a further oxidation of the cluster to the C_{red1} redox state. Indeed, as discussed above, when His93 is singly protonated, such a step results in the transfer of electron density from CO_2 to the C-cluster that makes its oxidation more favorable. Calculations of $E_{red} - E_{ox}$ energy differences for μCO_2 and tCO_2 adducts confirm this picture. Since the oxidation and reduction potentials for a given species are identical in value but opposite in sign, $-(E_{red} - E_{ox})$ values are expected to provide an estimate of the oxidation potentials. The $-(E_{red} - E_{ox})$ value computed for $\mathbf{C_{int}\text{-}tCO_2}$ $(\mathbf{H^0,K^+})$ is less positive (i.e., the oxidation potential is more positive) than that calculated for $\mathbf{C_{int}\text{-}\mu CO_2}$ $(\mathbf{H^0,K^+})$ by about 0.28 eV (see Table S13). Oxidation of $\mathbf{C_{int}\text{-}tCO_2}$ $(\mathbf{H^0,K^+})$ therefore requires potentials less positive than those needed for oxidation of $\mathbf{C_{int}\text{-}\mu CO_2}$ $(\mathbf{H^0,K^+})$.

The release of CO_2 from $\mathbf{C_{red1}\text{-}tCO_2}$ $(\mathbf{H^0,K^+})$ to give the unbound form of the C-cluster in a strongly exoergic process (−13.1 kcal/mol) is questionable. In the C_{red1} redox state a H_2O/OH^- ligand is indeed expected to occupy the vacant site at the Fe_u atom that is created upon μCO_2 to tCO_2 isomerization. Interestingly, in the C_{red1} state, the binding of a H_2O molecule, initially H-bonded to His93 and Lys563, to Fe_u and the transfer of one of its hydrogen atoms to His93 to give a CO_2-OH adduct is exoergic by 4.6 kcal/mol. In C_{int} and C_{red2}, such a process is instead endoergic by 2.2 and 7.1 kcal/mol, respectively (see Scheme 2). Subsequent CO_2 release from C_{red1}-CO_2-OH, yielding the OH-bound form of the C-cluster in C_{red1}, is energetically favored by 5.3 kcal/mol.

As shown in Schemes 3 and 4, the His93 residue is proposed to be involved in proton transfers from/to the C-cluster both in the binding and in the release of CO_2 from the active site. In this respect, it is worth noting that the involvement of His93 in such processes is more likely than that of Lys563. Indeed, in all redox states investigated, the unbound form of the C-cluster in which His93 is deprotonated ($LM^{H0,K+}$) is slightly more stable than the corresponding species in which deprotonation occurs at Lys563 ($LM^{H+,K0}$) (5.7, 1.7, and 3.2 kcal/mol in the C_{red2}, C_{int}, and C_{red1} states, respectively). Conversely, during geometry optimization of the OH-bound forms of the C-cluster in the C_{int} and C_{red2} redox states with the $LM^{H+,K+}$ model a proton is spontaneously transferred from His93 to the OH^- ligand. On the other hand, optimization of C_{red1}-OH with the $LM^{H+,K0}$ model results in the spontaneous transfer of a proton from His93 to OH^- and then to Lys563. This process can be explained by an analysis of the geometry of the system. The removal from Lys563 of the proton pointing toward the $NiFe_u$ site indeed produces a strong electrostatic repulsion between the N atom of Lys563 and the oxygen atom of OH^-. Analogously, if one of the other two protons of Lys563 is removed, the N_{Lys563} atom is repulsed by lone pairs of nearby residues (in particular, either the O atom of the carboxamide group of Gln332 or the S atom of Cys333). To avoid the formation of such unfavorable interactions, the system prefers to deprotonate His93. Furthermore, the reciprocal orientation of OH^- and His93 allows the formation of a strong H bond between the deprotonated εN atom of His93 and the hydrogen atom of the hydroxide ligand. All of these results strongly suggest that the deprotonation of His93 is more feasible than that of Lys563.

CONCLUSIONS

The disclosure of the stereoelectronic and catalytic properties of the active site of Ni,Fe-containing carbon monoxide dehydrogenases is important not only in the context of the efforts aimed at elucidating structure−function relationships but also for the development of bioinspired catalysts for CO_2/CO interconversion that may be used for the removal of such gases from the environment. To contribute to such an effort, the mechanism of binding and dissociation of CO_2 to/from the C-cluster has been investigated.

A comparison of results obtained using a minimal DFT model (metal ions and first coordination sphere) and a very large model of the active site (metal cluster, first and second coordination spheres; 270 atoms) highlights the crucial role of the His93 and Lys563 residues in tuning the coordination geometry of the C-cluster and the stability of CO_2 adducts. His93 and Lys563 residues are also both shown to be involved in proton transfers from/to the C-cluster. Mutational studies on *Mt*CODH[27] confirm the fundamental role of such residues. Indeed, the enzyme activity is significantly attenuated in mutants in which His93 and Lys563 are individually changed to alanine, whereas it is abolished in the double mutant. The latter result indicates that His93 and Lys563 are involved in catalysis of CODH serving the same function. Our calculations suggest, however, that the catalytic cycle more likely involves proton transfers from/to the C-cluster and His93. Still, in consideration mainly of the high flexibility and spatial extension of the Lys side chain, elucidation of the aforementioned reciprocal compensation of the latter residue for the former will require further theoretical investigations based on an explicit treatment of the dynamic properties of the active site's second coordination sphere.

The protonation state of His93 is also predicted to highly influence the direction in which the CO_2/CO interconversion occurs; the charged protonated form of His93 indeed favors the binding of CO_2, whereas the neutral form of this residue, in which only the δN atom is protonated, promotes its release. The redox state of the C-cluster is also shown to affect the energetics of the chemical binding and dissociation of CO_2. In particular, binding and release of CO_2 are respectively favored by the reduction and oxidation of the active site.

On the basis of these results, a mechanism for CO_2 binding and CO_2 release to/from the C-cluster has been proposed. CO_2 initially binds, according to a dissociative mechanism, to the terminal position of the Ni atom of the C-cluster in the C_{red2} state when His93 is doubly protonated. Subsequent displacement of CO_2 to the bridging position of the Ni-Fe_u site leads to the formation of the well-characterized CO_2 adduct of the C-cluster.[5,19] Our calculations, however, also support the non-catalytic binding of CO_2 to the OH-bound form of the C-cluster in the C_{red1} state according to an associative mechanism.[57]

While binding of CO_2 is a strongly favored process, the dissociation of CO_2 from the active site according to both dissociative and associative mechanisms is predicted to be more complex. Oxidation of the C-cluster at least to the C_{int} redox state and the endoergic μCO_2 to tCO_2 isomerization are required. Accordingly, NMR and steady-state kinetic studies showed that the release of CO_2 is partially rate limiting.[59] In such experiments, after the binding of CO to the C-cluster and its oxidation to CO_2, bound CO_2 is reduced back to CO that then dissociates from the active site. The rate of CO_2 release has been shown therefore to be slower than the rate of cluster reduction.

ASSOCIATED CONTENT

Supporting Information

The Supporting Information is available free of charge at https://pubs.acs.org/doi/10.1021/acs.inorgchem.0c03034.

https://dx.doi.org/10.1021/acs.inorgchem.0c03034
Inorg. Chem. 2021, 60, 387−402

Detailed information list of the atoms composing the active site models, list of the selected atoms that, during geometry optimizations, have been constrained to the crystallographic positions to avoid unrealistic distortions at the boundary of the model, structural details and electronic structure properties of selected species, and energies of all species investigated in this work (PDF)

AUTHOR INFORMATION

Corresponding Authors

Claudio Greco − *Department of Earth and Environmental Sciences, University of Milano-Bicocca, 20126 Milan, Italy;* orcid.org/0000-0001-9628-7875; Email: claudio.greco@unimib.it

Luca De Gioia − *Department of Biotechnology and Biosciences, University of Milano-Bicocca, 20126 Milan, Italy;* Email: luca.degioia@unimib.it

Authors

Raffaella Breglia − *Department of Earth and Environmental Sciences, University of Milano-Bicocca, 20126 Milan, Italy;* orcid.org/0000-0003-0579-8552

Federica Arrigoni − *Department of Biotechnology and Biosciences, University of Milano-Bicocca, 20126 Milan, Italy*

Matteo Sensi − *Department of Biotechnology and Biosciences, University of Milano-Bicocca, 20126 Milan, Italy;* orcid.org/0000-0002-0491-7161

Piercarlo Fantucci − *Department of Biotechnology and Biosciences, University of Milano-Bicocca, 20126 Milan, Italy*

[‖]**Maurizio Bruschi** − *Department of Earth and Environmental Sciences, University of Milano-Bicocca, 20126 Milan, Italy;* orcid.org/0000-0002-5709-818X

Complete contact information is available at: https://pubs.acs.org/10.1021/acs.inorgchem.0c03034

Author Contributions

The manuscript was written through contributions of all authors. All authors have given approval to the final version of the manuscript.

Notes

The authors declare no competing financial interest.

[‖]Deceased.

ACKNOWLEDGMENTS

We acknowledge CINECA for the availability of high-performance computing resources as part of the agreement with the University of Milano-Bicocca.

REFERENCES

(1) Ensign, S. A. Reactivity of Carbon Monoxide Dehydrogenase from Rhodospirillum Rubrum with Carbon Dioxide, Carbonyl Sulfide, and Carbon Disulfide. *Biochemistry* **1995**, *34*, 5372−5381.

(2) Svetlitchnyi, V.; Peschel, C.; Acker, G.; Meyer, O. Two Membrane-Associated NiFeS-Carbon Monoxide Dehydrogenases from the Anaerobic Carbon-Monoxide-Utilizing Eubacterium Carboxydothermus Hydrogenoformans. *J. Bacteriol.* **2001**, *183*, 5134−5144.

(3) Dobbek, H.; Gremer, L.; Kiefersauer, R.; Huber, R.; Meyer, O. Catalysis at a Dinuclear [CuSMo(=O)OH] Cluster in a CO Dehydrogenase Resolved at 1.1-Å Resolution. *Proc. Natl. Acad. Sci. U. S. A.* **2002**, *99*, 15971−15976.

(4) Hille, R.; Dingwall, S.; Wilcoxen, J. The Aerobic CO Dehydrogenase from Oligotropha Carboxidovorans. *JBIC, J. Biol. Inorg. Chem.* **2015**, *20*, 243−251.

(5) Jeoung, J. H.; Dobbek, H. Carbon Dioxide Activation at the Ni,Fe-Cluster of Anaerobic Carbon Monoxide Dehydrogenase. *Science* **2007**, *318*, 1461−1464.

(6) Darnault, C.; Volbeda, A.; Kim, E. J.; Legrand, P.; Vernède, X.; Lindahl, P. a; Fontecilla-Camps, J. C. Ni-Zn-[Fe4-S4] and Ni-Ni-[Fe4-S4] Clusters in Closed and Open α Subunits of Acetyl-CoA Synthase/Carbon Monoxide Dehydrogenase. *Nat. Struct. Mol. Biol.* **2003**, *10*, 271−279.

(7) Doukov, T. I.; Iverson, T. M.; Seravalli, J.; Ragsdale, S. W.; Drennan, C. L. A Ni-Fe-Cu Center in a Bifunctional Carbon Monoxide Dehydrogenase/Acetyl-CoA Synthase. *Science* **2002**, *298*, 567−572.

(8) Hu, Z.; Spangler, N. J.; Anderson, M. E.; Xia, J.; Ludden, P. W.; Lindahl, P. A.; Münck, E. Nature of the C-Cluster in Ni-Containing Carbon Monoxide Dehydrogenases. *J. Am. Chem. Soc.* **1996**, *118*, 830−845.

(9) Spangler, N. J.; Meyers, M. R.; Gierke, K. L.; Kerby, R. L.; Roberts, G. P.; Ludden, P. W. Substitution of Valine for Histidine 265 in Carbon Monoxide Dehydrogenase from Rhodospirillum Rubrum Affects Activity and Spectroscopic States. *J. Biol. Chem.* **1998**, *273*, 4059−4064.

(10) Ralston, C. Y.; Wang, H.; Ragsdale, S. W.; Kumar, M.; Spangler, N. J.; Ludden, P. W.; Gu, W.; Jones, R. M.; Patil, D. S.; Cramer, S. P. Characterization of Heterogeneous Nickel Sites in CO Dehydrogenases from Clostridium Thermoaceticum and Rhodospirillum Rubrum by Nickel L-Edge X-Ray Spectroscopy. *J. Am. Chem. Soc.* **2000**, *122*, 10553−10560.

(11) Kung, Y.; Drennan, C. L. A Role for Nickel-Iron Cofactors in Biological Carbon Monoxide and Carbon Dioxide Utilization. *Curr. Opin. Chem. Biol.* **2011**, *15*, 276−283.

(12) Can, M.; Armstrong, F. A.; Ragsdale, S. W. Structure, Function, and Mechanism of the Nickel Metalloenzymes, CO Dehydrogenase, and Acetyl-CoA Synthase. *Chem. Rev.* **2014**, *114*, 4149−4174.

(13) Lindahl, P. A. Implications of a Carboxylate-Bound C-Cluster Structure of Carbon Monoxide Dehydrogenase. *Angew. Chem., Int. Ed.* **2008**, *47*, 4054−4056.

(14) Amara, P.; Mouesca, J. M.; Volbeda, A.; Fontecilla-Camps, J. C. Carbon Monoxide Dehydrogenase Reaction Mechanism: A Likely Case of Abnormal CO2 Insertion to a Ni-H- Bond. *Inorg. Chem.* **2011**, *50*, 1868−1878.

(15) Gu, W. W.; Seravalli, J.; Ragsdale, S. W.; Cramer, S. P. CO-Induced Structural Rearrangement of the C-Cluster in Carboxydothermus Hydrogenformans CO Dehydrogenase - Evidence from Ni K-Edge X-Ray Absorption Spectroscopy. *Biochemistry* **2004**, *43*, 9029−9035.

(16) Wilcoxen, J.; Zhang, B.; Hille, R. Reaction of the Molybdenum- and Copper-Containing Carbon Monoxide Dehydrogenase from Oligotropha Carboxydovorans with Quinones. *Biochemistry* **2011**, *50*, 1910−1916.

(17) Volbeda, A.; Fontecilla-Camps, J. C. Structural Bases for the Catalytic Mechanism of Ni-Containing Carbon Monoxide Dehydrogenases. *Dalt. Trans.* **2005**, 3443−3450.

(18) Appel, A. M.; Bercaw, J. E.; Bocarsly, A. B.; Dobbek, H.; Dubois, D. L.; Dupuis, M.; Ferry, J. G.; Fujita, E.; Hille, R.; Kenis, P. J. A.; et al. Frontiers, Opportunities, and Challenges in Biochemical and Chemical Catalysis of CO2 Fixation. *Chem. Rev.* **2013**, *113*, 6621−6658.

(19) Fesseler, J.; Jeoung, J. H.; Dobbek, H. How the [NiFe4S4] Cluster of CO Dehydrogenase Activates CO2 and NCO-. *Angew. Chem., Int. Ed.* **2015**, *54*, 8560−8564.

(20) Liao, R.-Z.; Siegbahn, P. E. M. Energetics for the Mechanism of Nickel-Containing Carbon Monoxide Dehydrogenase. *Inorg. Chem.* **2019**, *58*, 7931−7938.

(21) Jeoung, J. H.; Dobbek, H. N-Butyl Isocyanide Oxidation at the [NiFe4S4OHx] Cluster of CO Dehydrogenase. *JBIC, J. Biol. Inorg. Chem.* **2012**, *17*, 167−173.

(22) Siegbahn, P. E. M.; Himo, F. Recent Developments of the Quantum Chemical Cluster Approach for Modeling Enzyme Reactions. *JBIC, J. Biol. Inorg. Chem.* **2009**, *14*, 643−651.

(23) Siegbahn, P. E. M.; Himo, F. The Quantum Chemical Cluster Approach for Modeling Enzyme Reactions. *Wiley Interdiscip. Rev. Comput. Mol. Sci.* **2011**, *1*, 323−336.

(24) Alberto, M. E.; Marino, T.; Russo, N.; Sicilia, E.; Toscano, M. The Performance of Density Functional Based Methods in the Description of Selected Biological Systems and Processes. *Phys. Chem. Chem. Phys.* **2012**, *14*, 14943−14953.
(25) Drennan, C. L.; Heo, J.; Sintchak, M. D.; Schreiter, E.; Ludden, P. W. Life on Carbon Monoxide: X-Ray Structure of Rhodospirillum Rubrum Ni-Fe-S Carbon Monoxide Dehydrogenase. *Proc. Natl. Acad. Sci. U. S. A.* **2001**, *98*, 11973−11978.
(26) Dobbek, H.; Svetlitchnyi, V.; Gremer, L.; Huber, R.; Meyer, O. Crystal Structure of a Carbon Monoxide Dehydrogenase Reveals a [Ni-4Fe-5S] Cluster. *Science* **2001**, *293*, 1281−1285.
(27) Kim, E. J.; Feng, J.; Bramlett, M. R.; Lindahl, P. A. Evidence for a Proton Transfer Network and a Required Persulfide-Bond-Forming Cysteine Residue in Ni-Containing Carbon Monoxide Dehydrogenases. *Biochemistry* **2004**, *43*, 5728−5734.
(28) Ahlrichs, R.; Bar, M.; Haser, M.; Horn, H.; Kolmel, C. Electronic Structure Calculations on Workstation Computers: The Program System Turbomole. *Chem. Phys. Lett.* **1989**, *162*, 165−169.
(29) Becke, A. D. Density-Functional Exchange-Energy Approximation with Correct Asymptotic Behavior. *Phys. Rev. A: At., Mol., Opt. Phys.* **1988**, *38*, 3098−3100.
(30) Perdew, J. P. Density-Functional Approximation for the Correlation Energy of the Inhomogeneous Electron Gas. *Phys. Rev. B: Condens. Matter Mater. Phys.* **1986**, *33*, 8822−8824.
(31) Eichkorn, K.; Treutler, O.; Ohm, H.; Haser, M.; Ahlrichs, R. Auxiliary Basis Sets to Approximate Coulomb Potentials. *Chem. Phys. Lett.* **1995**, *240*, 283−290.
(32) Jonas, V.; Thiel, W. Theoretical Study of the Vibrational Spectra of the Transition Metal Carbonyls M(CO)6 [M = Cr, Mo, W], M(CO)5 [M = Fe, Ru, Os], and M(CO)4 [M = Ni, Pd, Pt]. *J. Chem. Phys.* **1995**, *102*, 8474−8484.
(33) Koch, W.; Holthausen, M. C. *A Chemist's Guide to Density Functional Theory*, 2nd ed.; Wiley-VCH: Weinheim, 2000.
(34) Schäfer, A.; Huber, C.; Ahlrichs, R. Fully Optimized Contracted Gaussian Basis Sets of Triple Zeta Valence Quality for Atoms Li to Kr. *J. Chem. Phys.* **1994**, *100*, 5829−5835.
(35) Schäfer, A.; Huber, C.; Ahlrichs, R. Fully Optimized Contracted Gaussian Basis Sets of Triple Zeta Valence Quality for Atoms Li to Kr. *J. Chem. Phys.* **1992**, *97*, 2571−2577.
(36) Klamt, A.; Schuurmann, G. COSMO: A New Approach to Dielectric Screening in Solvents with Explicit Expressions for the Screening Energy and Its Gradient. *J. Chem. Soc., Perkin Trans. 2* **1993**, *0*, 799−805.
(37) Klamt, A. Conductor-like Screening Model for Real Solvents: A New Approach to the Quantitative Calculation of Solvation Phenomena. *J. Phys. Chem.* **1995**, *99*, 2224−2235.
(38) Greco, C.; Ciancetta, A.; Bruschi, M.; Kulesza, A.; Moro, G.; Cosentino, U. Influence of Key Amino Acid Mutation on the Active Site Structure and on Folding in Acetyl-CoA Synthase: A Theoretical Perspective. *Chem. Commun.* **2015**, *51*, 8551−8554.
(39) Greco, C.; Fantucci, P.; Ryde, U.; De Gioia, L. Fast Generation of Broken-Symmetry States in a Large System Including Multiple Iron−Sulfur Assemblies: Investigation of QM/MM Energies, Clusters Charges, and Spin Populations. *Int. J. Quantum Chem.* **2011**, *111*, 3949−3960.
(40) Becke, A. D. Density-Functional Thermochemistry. III. The Role of Exact Exchange. *J. Chem. Phys.* **1993**, *98*, 5648−5652.
(41) Lee, C.; Yang, W.; Parr, R. G. Development of the Colle-Salvetti Correlation-Energy Formula into a Functional of the Electron Density. *Phys. Rev. B: Condens. Matter Mater. Phys.* **1988**, *37*, 785−789.
(42) Stephens, P. J.; Devlin, F. J.; Chabalowski, C. F.; Frisch, M. J. Ab Initio Calculation of Vibrational Absorption and Circular Dichroism Spectra Using Density Functional Force Fields. *J. Phys. Chem.* **1994**, *98*, 11623−11627.
(43) Adamo, C.; Scuseria, G. E.; Barone, V. Accurate Excitation Energies from Time-Dependent Density Functional Theory: Assessing the PBE0Model. *J. Chem. Phys.* **1999**, *111*, 2889−2899.
(44) Zhao, Y.; Truhlar, D. G. The M06 Suite of Density Functionals for Main Group Thermochemistry, Thermochemical Kinetics, Noncovalent Interactions, Excited States, and Transition Elements: Two New Functionals and Systematic Testing of Four M06-Class Functionals and 12 Other Function. *Theor. Chem. Acc.* **2008**, *120*, 215−241.
(45) Grimme, S.; Antony, J.; Ehrlich, S.; Krieg, H. A Consistent and Accurate Ab Initio Parametrization of Density Functional Dispersion Correction (DFT-D) for the 94 Elements H-Pu. *J. Chem. Phys.* **2010**, *132*, 154104−154119.
(46) Grimme, S. Accurate Description of van Der Waals Complexes by Density Functional Theory Including Empirical Corrections. *J. Comput. Chem.* **2004**, *25*, 1463−1473.
(47) Grimme, S. Semiempirical GGA-Type Density Functional Constructed with a Long-Range Dispersion Correction. *J. Comput. Chem.* **2006**, *27*, 1787−1799.
(48) Grimme, S.; Ehrlich, S.; Goerigk, L. Effect of the Damping Function in Dispersion Corrected Density Functional Theory. *J. Comput. Chem.* **2011**, *32*, 1456−1465.
(49) Goerigk, L.; Kruse, H.; Grimme, S. Benchmarking Density Functional Methods against the S66 and S66 × 8 Datasets for Non-Covalent Interactions. *ChemPhysChem* **2011**, *12*, 3421−3433.
(50) Weymuth, T.; Couzijn, E. P. A.; Chen, P.; Reiher, M. New Benchmark Set of Transition-Metal Coordination Reactions for the Assessment of Density Functionals. *J. Chem. Theory Comput.* **2014**, *10*, 3092−3103.
(51) Noodleman, L. Valence Bond Description of Antiferromagnetic Coupling in Transition Metal Dimers. *J. Chem. Phys.* **1981**, *74*, 5737−5743.
(52) Lindahl, P. A. The Ni-Containing Carbon Monoxide Dehydrogenase Family: Light at the End of the Tunnel? *Biochemistry* **2002**, *41*, 2097−2105.
(53) Kung, Y.; Doukov, T. I.; Seravalli, J.; Ragsdale, S. W.; Drennan, C. L. Crystallographic Snapshots of Cyanide- and Water-Bound C-Clusters from Bifunctional Carbon Monoxide Dehydrogenase/Acetyl-CoA Synthase. *Biochemistry* **2009**, *48*, 7432−7440.
(54) DeRose, V. J.; Telser, J.; Anderson, M. E.; Lindahl, P. A.; Hoffman, B. M. A Multinuclear ENDOR Study of the C-Cluster in CO Dehydrogenase from Clostridium Thermoaceticum: Evidence for HxO and Histidine Coordination to the [Fe4S4] Center. *J. Am. Chem. Soc.* **1998**, *120*, 8767−8776.
(55) Anderson, M. E.; Lindahl, P. A. Organization of Clusters and Internal Electron Pathways in CO Dehydrogenase from Clostridium Thermoaceticum: Relevance to the Mechanism of Catalysis and Cyanide Inhibition. *Biochemistry* **1994**, *33*, 8702−8711.
(56) Fraser, D. M.; Lindahl, P. A. Evidence for a Proposed Intermediate Redox State in the CO/CO2 Active Site of Acetyl-CoA Synthase (Carbon Monoxide Dehydrogenase) from Clostridium Thermoaceticum. *Biochemistry* **1999**, *38*, 15706−15711.
(57) Anderson, M. E.; Lindahl, P. A. Spectroscopic States of the CO Oxidation/CO2 Reduction Active Site of Carbon Monoxide Dehydrogenase and Mechanistic Implications. *Biochemistry* **1996**, *35*, 8371−8380.
(58) Heo, J.; Staples, C. R.; Ludden, P. W.; Recei, V.; No, V. Redox-Dependent CO2 Reduction Activity of CO Dehydrogenase from Rhodospirillum Rubrum. *Biochemistry* **2001**, *40*, 7604−7611.
(59) Seravalli, J.; Ragsdale, S. W. 13C NMR Characterization of an Exchange Reaction between CO and CO2 Catalyzed by Carbon Monoxide Dehydrogenase. *Biochemistry* **2008**, *47*, 6770−6781.

https://dx.doi.org/10.1021/acs.inorgchem.0c03034
Inorg. Chem. 2021, 60, 387−402